PREPARATION AND INVESTIGATION OF FREQUENCY DEPENDENCE PERMEABILITY OF Co-Zn FERRITE

A Dissertation Submitted to the Department of Physics,
Bangladesh University of Engineering & Technology, Dhaka, in
Partial Fulfillment of the Requirement for the Degree of
Master of Philosophy in Physics

Submitted by

Kazi Khirul Kabir

EXAMINATION ROLL NO. : 0404140026F
REGISTRATION NO. : 0404553
SESSION : April - 2004

DEPARTMENT OF PHYSICS

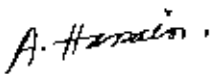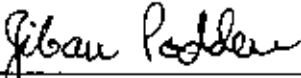BANGLADESH UNIVERSITY OF ENGINEERING & TECHNOLOGY

DHAKA 1000, BANGLADESH

BANGLADESH UNIVERSITY OF ENGINEERING & TECHNOLOGY
DEPARTMENT OF PHYSICS, DHAKA 1000, BANGLADESH
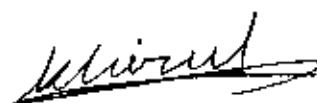
CERTIFICATION OF THESIS

The thesis titled "**Preparation and Investigation of Frequency Dependence Permeability of Co-Zn Ferrite**" submitted by **Kazi Khirul Kabir**, Roll No.: 040414026F, Session: April 2004, has been accepted as satisfactory in partial fulfillment of the requirement for the degree of **Master of Philosophy** in Physics on December 24, 2006.

BOARD OF EXAMINERS

1. (_A. Hossain_)   Chairman
   Dr. A. K. M. Akther Hossain (Supervisor)
   Associate Professor. Department of Physics
   BUET.

2. (_Jiban Podder_)   Member
   Dr. Jiban Podder, Professor and Head.
   Department of Physics. BUET.

3. (_mnIslam_)   Member
   Dr. Md. Nazrul Islam, Associate Professor
   Department of Physics, BUET.

4. (_Kamal_)   Member
   Dr. Md. Kamal-Al-Hassan.   (External)
   Assistant Professor & Head
   Department of Physics
   Dhaka University of Engineering & Technology (DUET)
   Gazipur 1700, Bangladesh.

III

CANDIDATE'S DECLARATION

It is hereby declared that this thesis or any part of it has not been submitted elsewhere for the award of any degree or diploma.

KAZI KHIRUL KABIR

ACKNOWLEDGMENTS

ABSTRACT

$Co_{1-x}Zn_xFe_2O_4$ with x=0.60 and 0.80 were prepared by a conventional solid state reaction technique. The samples were sintered at various temperatures (1100°C, 1150°C 1200°C, 1250°C and 1300°C) in air for 5 hours and at 1200°C in air for various durations (0.2h, 1h, 5h, 10h and 15h). Structural and surface morphology were studied by x-ray diffraction and optical microscopy. The magnetic properties of the ferrites were characterized with frequency dependence complex permeability at room temperature and temperature dependent permeability measurements at 100 KHz. The effects of microstructure, composition, sintering temperature and sintering time on the complex permeability of Co-Zn ferrite are discussed. A possible correlation among sintering temperature, sintering time, grain size, density and porosity is also discussed. The X-ray diffraction patterns of both compositions clearly indicate their single phase and formation of spinel structure. The lattice constant of $Co_{0.40}Zn_{0.60}Fe_2O_4$ is found to be 8.4528 Å while 8.4644 Å for $Co_{0.20}Zn_{0.80}Fe_2O_4$. The increase in lattice parameter with increasing Zn content can be explained on the basis of the ionic radii. The radius of the Zn^{2+} (0.74 Å) is greater than that of the Co^{2+} (0.72 Å). The microstructure study shows that grain size increases with increasing zinc substitution. The average grain sizes for the both compositions are determined by linear intercept technique. The bulk density of the $Co_{0.40}Zn_{0.60}Fe_2O_4$ samples increases as the sintering temperature (T_s) increases from 1100°C to 1250°C, and above 1250°C the bulk density decreases slightly. The $Co_{0.20}Zn_{0.80}Fe_2O_4$ samples show similar behaviors of changes to that of $Co_{0.40}Zn_{0.60}Fe_2O_4$ samples except that the bulk density is found to be highest at 1200°C. During the sintering process, the thermal energy generates a force that drives the grain boundaries to grow over pores, thereby decreasing the pore volume and increasing the density of the material. At higher sintering temperatures, the density decreases because the intragranular porosity increases resulting from discontinuous grain growth. The initial permeability proportionally changes with density of the samples. A sample with more uniformity as well as highest density is obtained for the sample sintered at 1250°C (optimum T_s) for $Co_{0.40}Zn_{0.60}Fe_2O_4$. The real part of initial permeability, μ_i' , is observed to be maximum at this optimum T_s for $Co_{0.40}Zn_{0.60}Fe_2O_4$. For both the compositions, μ_i'

is found to be maximum at optimum T_s (depending on sample composition). If the sintering temperature is higher than that of the optimum T_s, μ_i' decreases. Higher sintering temperatures (> optimum T_s) may increase the number of pores within the grains of the samples which result in a decrease in permeability. The ferrite with high permeability tends to have its permeability decreases at a relatively low frequency. The μ_i' values for all samples are found independent of frequency because μ_i' is independent of frequency below the resonance frequency and in our research we did not find the resonance frequency below 13MHz . The highest relative quality factor (Q) for $Co_{0.40}Zn_{0.60}Fe_2O_4$ is found to be 2.25×10^3 at frequency 4MHz at 1300°C sintering temperature. While the Q value for $Co_{0.20}Zn_{0.80}Fe_2O_4$ samples are not found because they lie above our frequency range (>13MHz). The DC magnetisation as a function of temperature curves show that the $Co_{0.40}Zn_{0.60}Fe_2O_4$ sample is ferrimagnetic at room temperature while the $Co_{0.20}Zn_{0.80}Fe_2O_4$ sample is paramagnetic at room temperature. The T_c of $Co_{0.20}Zn_{0.80}Fe_2O_4$ sample is found to be 170K from DC magnetisation measurement. Separate measurement (AC magnetisation), initial permeability as a function of temperature shows that the T_c of the $Co_{0.40}Zn_{0.60}Fe_2O_4$ samples is about 353 K. Slight variation of T_c is observed depending on sintering condition. The initial permeability of the samples as a function of temperature is measured at a constant frequency (100 kHz) of a sinusoidal wave.

CONTENTS

CHAPTER 1

GENERAL INTRODUCTION   1-4

CHAPTER 2

REVIEW OF MAGNETIC PROPERTIES OF FERRITES   5-35

CHAPTER 3

SAMPLE PREPARATION AND STRUCTURAL CHARACTERIZATION 36-42

CHAPTER 4

EXPERIMENTAL TECHNIQUES 43-47

CHAPTER 5

RESULTS AND DISCUSSION

48-70

CHAPTER 6

CONCLUSIONS

72-75

LIST OF FIGURES

LIST OF TABLES

LIST OF SYMBOLS AND ABBREVIATIONS

AC	Alternating current
B	Magnetic induction
CMR	Colossal magnetoresistance
$F(\theta)$	Nelson-Riley function
f_r	Resonance frequency
g	Landé splitting factor
H_{c}	Critical field
J	Exchange integral
K	Total anisotropy
K_1	Magnetocrystalline anisotropy constant
L_s	Self-inductance of the sample core
L_o	Inductance of the winding coil without sample
M	Magnetization
M_s	Saturation magnetization
N_A	Avogadro's number
P	Porosity
P_{intra}	Intragranular porosity
P_{inter}	Intergranular porosity
P_e	Eddy-current loss
Q	Relative quality factor
T_c	Curie temperature
T_n	Néel temperature
T_s	Sintering temperature
$tan\delta$	Loss factor
Z	Complex impedance
α	Restoring force coefficient
β	Viscous damping factor
γ	Domain wall energy
ω	Angular velocity
δ_w	Domain wall thickness
μ_i	Initial permeability
μ'	Real part of complex permeability
μ''	Imaginary part of complex permeability
μ_B	Bohr magneton
χ_{spin}	Intrinsic rotational susceptibility
χ_w	Domain wall susceptibility

CHAPTER 1

GENERAL INTRODUCTION

1.1 Introduction

Ferrites are ceramic materials formed by reacting metal oxides into magnetic materials. These are soft magnetic materials that can be both easily magnetized and demagnetized, so that it can store or transfer magnetic energy in alternating or other changing wave forms (i.e. sine, pulse, square, etc). According to their structure spinel-type ferrites are natural superlattices. It has tetrahedral A site and octahedral B site in AB_2O_4 crystal structure. It shows various magnetic properties depending on the composition and cation distribution. Various cations can be placed in A site and B site to tune its magnetic properties. Depending on A site and B site cations it can exhibit ferrimagnetic, antiferromagnetic, spin (cluster) glass, and paramagnetic behavior [1, 2]. Due to their remarkable behavior of magnetic and electric properties they are subjects of intense theoretical and experimental investigation for application purpose [2-6]. These polycrystalline spinel ferrites are widely used in many electronic devices. They are preferred because of their high permeability and saturation magnetization in the radio-frequency (RF) region, high electrical resistivity, mechanical hardness and chemical stability [7]. Ferrites are also useful to prevent and eliminate RF interference to audio systems [8]. Most other technologically useful magnetic materials such as iron and soft magnetic alloys have low electrical resistivity. This makes them useless for applications at high frequencies, for example as inductor core in TV circuits. The problem is that their low electrical resistivity allows eddy currents to flow within the materials themselves, thereby producing heat. This is wasted energy and the produced heat is often a serious problem [9-14]. Thus, non-ferrite materials become inefficient as they waste energy and the waste is more, as the frequency becomes higher. In this paper, we report preparation and investigation of frequency dependence permeability of $Co_{1-x}Zn_xFe_2O_4$ (x=0.60, 0.80) samples sintered at various temperatures (1100-1300°C), and various durations (0.2h-15h). We also discus about structural and DC magnetic properties of $Co_{1-x}Zn_xFe_2O_4$ (x=0.60, 0.80) samples. In view of the importance of high

frequency devices, we have analyzed AC magnetic behaviour of samples at high frequency (1kHz-13MHz). Possible explanation for the observed characteristics of magnetization and initial permeability of the studied samples are discussed.

1.2 Objectives of the Present Work

Ferrites are especially convenient for high frequency uses because of their high resistivity. The high frequency response of the complex permeability is therefore very useful in determining the convenient frequency range in which a particular ferrite material can be used. The mechanism of eddy current losses and damping of domain wall motion can be understood from the relative magnitudes of the real and imaginary parts of the complex permeability. The effect of composition and microstructure on the frequency response is therefore very useful.

The main *objectives* of the present research are as follows:

- Preparation of various $Co_{1-x}Zn_xFe_2O_4$ (for x=0.60 and 0.80) samples.
- Perform structural characterizations, density and porosity of the samples.
- Study of surface morphology (grain size).
- Initial permeability as a function of frequency (1KHz-13MHz).
- Investigation of DC magnetization.
- Determination of ferrimagnetic to paramagnetic transition temperature (T_c) from the measurement of temperature dependent initial permeability (μ_i).

Possible outcome of the research is as follows:

- From the sintering temperature (T_s) dependent permeability studies, an optimum T_s may be obtained for corresponding ferrite composition.
- A scaling of Curie temperature (T_c) with respect to sintering condition may be obtained, which will be helpful for practical applications of the above mentioned ferrites.

1.3 Summary of the Thesis

The format of the thesis is as follows:

Chapter 1 of this thesis deals with the importance of ferrites and objectives of the present work.

Chapter 2 gives a brief overview of the materials, theoretical background as well as crystal structure of the spinel type ferrites.

Chapter 3 gives the details of the sample preparation

Chapter 4 describes the descriptions of different measurements that have been used in this research work.

Chapter 5 is devoted to the results of various investigations of the study and explanation of results in the light of existing theories.

The conclusions drawn from the overall experimental results and discussion are presented in Chapter 6.

References

[1] R. Peelamedu, C. Grimes, D. Agrawal, and R. Roy, "Ultralow dielectric constant nickel-zinc ferrites using microwave sintering," *J. Mater. Res.*, **18**, 2292 (2003).

[2] A. K. M. Akther Hossain, S. T. Mahmud, M. Seki, T. Kawai and H. Tabata, "Structural, Electrical transport and Magnetic Properties of $Ni_{1-x}Zn_xFe_2O_4$," *Journal of magnetism and magnetic materials*, 2006, in press.

[3] A. Goldman, *Handbook of Modern Ferromagnetic Materials*, Kulwer Acad. Pub. Boston. U.S.A (1999).

[4] R. Valenzuela, *Magnetic Ceramics* Cambridge University Press. Cambridge (1994)

[5] L. K. Leung, B. J. Evans and A. H. Morrish, "Low-temperature Mössbauer study of a nickel-zinc ferrite: $Zn_{1-x}Ni_xFe_2O_4$," *Phys. Rev. B*, **8**, 29 (1973).

[6] W. Schiessl, W. Potzel, H. Karzel, M. Steiner and G. M. Kalvius, "Magnetic properties of the $ZnFe_2O_4$ spinel," *Phys. Rev. B*, **53**, 9143 (1996)

[7] J. M. Hasting and L. M. Corliss, "An antiferromagnetic transition in zinc ferrite," *Phys. Rev.* **102**, 1460 (1956).

[8] J. M. Hasting and L. M. Corliss, "Neutron diffraction studies of zinc ferrite and nickel ferrite," *Rev. Mod. Phys.*, **15**, 114 (1953)

[9] Yu. G. Chukalkin and A. E. Teplykh, "Magnetic state of nickel-zinc ferrites at high zinc concentrations," *Phys. Solid State*, **40**(8), 1364 (1998).

[10] M. A. Ahmed, N. Okasa and L. Salah, "Influence of yttrium ions on the magnetic properties of Ni-Zn ferrites," *Journal of Magnetism and Magnetic Materials*, **264**, 241 (2003).

[11] N. Rezlescu, E. Rezlescu, C. Pasnicu and M. L. Craus, "Effects of the rare-earth ions on some properties of a nickel-Zinc ferrite," *J. Phys.: Condens. Matter*, **6**, 5707 (1994)

[12] O. F. Caltun, L. Spinu and A. Stancu, "Structure and magnetic properties of Ni-Zn-Cu ferrites sintered at different temperatures," *Journal of Optoelectronics and Advanced Materials*, **4**(2), 337 (2002).

[13] A. Gonochar, V. Andreev, L. Letyuk, A. Shishkanov and V. Maiorov, "Problems of increasing of thermostability of highly permeable Ni-Zn ferrites and relative materials for communications," *Journal of Magnetism and Magnetic Materials*, **254**, 544 (2003).

[14] S. T. Mahmud, A. K. M. Akther Hossain, A. K. M. Abdul Hakim, M. Seki, T. Kawai and H. Tabata, "Influence of microstructure on the complex permeability of spinel type Ni-Zn ferrite," *Journal of Magnetism and Magnetic Materials*, **305**, 269 (2006).

CHAPTER 2

REVIEW OF MAGNETIC PROPERTIES OF FERRITES

Double oxides of iron and other metals are important members of ferrimagnetic system commonly known as ferrites The outstanding properties of ferrites are their high permeability and high electrical resistivity in the radio-frequency region In this chapter we describe a brief overview of the ferrites The basic issue of ferrimagnetism, crystal structure of the spinel ferrites and effect of non-magnetic Zn substitution on the magnetic moments in spinel ferrites are discussed A few theoretical aspects of complex permeability are also discussed.

2.1 Overview of the Materials

Ferrites commonly expressed by the general chemical formula $MeO\,Fe_2O_3$, where Me represents divalent metals, first commanded the public attention when Hilpert (1909) focused on the usefulness of ferrites at high frequency [1]. A systematic investigation was launched by Snoek (1936) at Philips Research Laboratory [2]. At the same time Takai (1937) in Japan was seriously engaged in the research work on the same materials [1]. Snoek's extensive works on ferrites unveiled many mysteries regarding magnetic properties of ferrites. He was particularly looking for high permeability materials of cubic structure. This particular structure for symmetry reasons supports low crystalline anisotropy. He found suitable materials in the form of mixed spinels of the type $MeZnFe_2O_3$, where Me stands for metals like Cu, Mg, Ni, Co or Mn for which permeability were found to be up to 4000 [1-3]. Here after starts the story of Co-Zn ferrites. Remarkable properties like high permeability, low loss factor, high stability of permeability with temperature and time, high wire resistance, controlled coercive force, low switching coefficient etc. have aptly placed Co-Zn ferrites as highly demandable ferrites to both researchers and manufacturers. Every year great deals of paper are being published on various aspects of Co-Zn ferrites. A large number of scientists and technologists are engaged in research to bring about improvements on the magnetic properties of Co-Zn ferrites.

The sintering process is considered to be one of the most vital steps in preparing ferrite samples and often plays a dominant role in many magnetic properties. Tasaki *et al.*

[4] studied the effect of sintering atmosphere on permeability of sintered ferrite. They found that high density of the sample is one of the factors, which contribute to greater permeability. However, permeability decreased in an atmosphere without O_2 at high sintering temperature where high density was expected. This decrease in permeability is attributed to the variation of chemical composition caused by volatilization of Zn. At low sintering temperature a high permeability is obtained in an atmosphere without O_2 because densification and stoichiometry plays a principal role in increasing permeability. At high sintering temperature the highest permeability is obtained in the presence of O_2 because the effect of decrease of Zn content can then be neglected.

Studying the electromagnetic properties of ferrites, Nakamura [5] suggested that both the density and the average grain size increased with sintering temperature. These changes were responsible for variations in magnetization, initial permeability and electrical resistivity.

High permeability attainment is certainly affected by the microstructure of the ferrites. Roess showed that [6] the very high permeability is restricted to certain temperature ranges and the shapes of permeability versus temperature curves are strongly affected by any inhomogeneity in the ferrite structure.

Rezlescu *et al* [7] reported that the sintering behaviour and microstructure of the ferrites samples largely affected by addition of PbO. PbO significantly reduced the sintering temperatures, thus energy consumption is minimized and material loss by evaporation is minimized [8].

There are two mechanisms in the phenomenon of permeability; spin rotation in the magnetic domains and wall displacements. The uncertainty of contribution from each of the mechanisms makes the interpretation of the experimental results difficult. Globus [9] shows that the intrinsic rotational permeability μ_r and 180^0 wall permeability μ_w may be written as: $\mu_r = 1 + 2\pi M_s^2 / K$ and $\mu_w = 1 + 3\pi M_s^2 D / 4\gamma$, where M_s is the saturation magnetization, K is the total anisotropy, D is the grain diameter and $\gamma = K\delta_w$ is the wall energy.

M. A. Ahmed et al [10] studied the DC, AC electrical resistivity of $Co_{0.20}Zn_{0.80}Fe_2O_4$ ferrites at high temperatures. The DC electrical resistivity (ρ_{dc})

decreases as temperature (T) of the sample increases. This decrease in the resistivity is due to the semiconductive behavior of the studied composition $Co_{0.20}Zn_{0.80}Fe_2O_4$ which is controlled by the form $\rho_{dc} = \rho_o exp(E/k_BT)$. Where ρ_o is the pre-exponential constant or resistivity at infinitely high temperature, k is Boltzmann's constant and E is the activation energy in eV for electrical conductions. The frequency dependence of the real AC electrical conductivity $(\sigma'_{ac}(\omega))$ increases as the frequency of the applied electric field increases. The relationship between the real AC electrical conductivity and the frequency can be written as $\sigma'_{ac}(\omega)=B\omega^n$, where B and n are constants which depend on both the temperature and composition and $\omega=2\pi f$ is the angular frequency.

2.2 Magnetic Ordering

The onset of magnetic order in solids has two basic requirements:

(i) Individual atoms should have magnetic moments (spins).

(ii) Exchange interactions should exist that couple them together.

Magnetic moments originate in solids as a consequence of overlapping of the electronic wave function with those of neighboring atoms. This condition is best fulfilled by some transition metals and rare-earths. The exchange interactions depend sensitively upon the inter-atomic distance and the nature of the chemical bonds, particularly of nearest neighbour atoms. When the positive exchange dominates, which corresponds to parallel coupling of neighbouring atomic moments (spins), the magnetic system becomes ferromagnetic below a certain temperature T_C called the Curie temperature. The common spin directions are determined by the minimum of magneto-crystalline anisotropy energy of the crystal. Therefore, ferromagnetic substances are characterized by spontaneous magnetization. But a ferromagnetic material in the demagnetized state displays no net magnetization in zero field because in the demagnetized state a ferromagnetic of macroscopic size is divided into a number of small regions called domains, spontaneously magnetized to saturation value and the directions of these spontaneous magnetization of the various domains are such that the net magnetization of the specimen is zero. The existence of domains is a consequence of energy minimization. The size and formation of these domains is in a complicated manner dependent on the shape of the specimen as well as its magnetic and thermal history. When negative exchange dominates, adjacent atomic moments (spins) align antiparallel

to each other, and the substance is said to be anti-ferromagnetic below a characteristic temperature, T_N, called the Néel temperature. In the simplest case, the lattice of an anti-ferromagnet is divided into two sublattices with the magnetic moments of these in anti-parallel alignment. The result is zero net magnetization. A special case of anti-ferromagnetism is ferrimagnetism. In ferrimagnetism, there are also two sublattices with magnetic moments in opposite directions, but the magnetization of the sublattices are of unequal strength resulting in a non-zero magnetization and therefore has net spontaneous magnetization. At the macroscopic level of domain structures, ferromagnetic and ferrimagnetic materials are therefore similar.
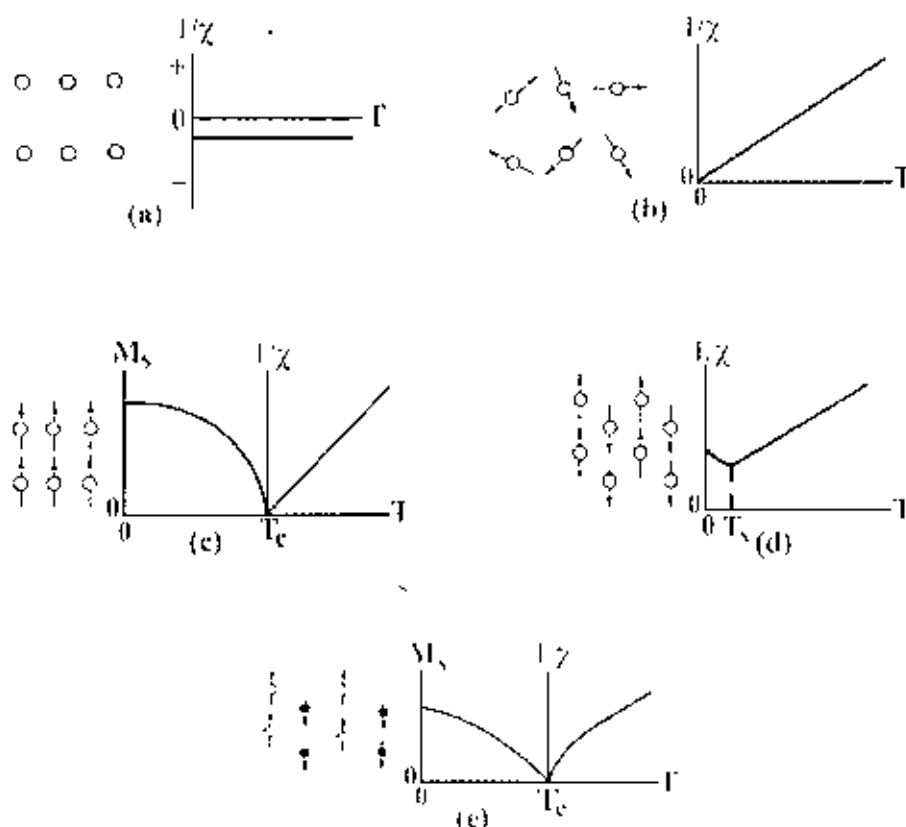
Figure 2.1. Temperature dependence of the inverse susceptibility for: (a) a diamagnetic material (b) a paramagnetic material, showing Curie's law behaviour, (c) a ferromagnetic material showing a spontaneous magnetization for $T<T_c$ and Curie-Weiss behaviour for $T>T_c$; (d) an antiferromagnetic material; (e) a ferrimagnetic material, showing a net spontaneous magnetization for $T<T_c$ and non linear behaviour for $T>T_c$.

The Curie and Néel temperatures characterize a phase transition between the magnetically ordered and disordered (paramagnetic) states. From these simple cases of magnetic ordering various types of magnetic order exists, particularly in metallic substances. Because of long-range order and oscillatory nature of the exchange interaction, mediated by the conduction electrons, structures like helical, conical and modulated patterns might occur. A useful property for characterizing the magnetic materials is the magnetic susceptibility, χ, defined as the magnetization, M, divided by the applied magnetic field, H i.e. $\chi = M / H$. The temperature dependence of susceptibility or, more accurately, inverse of susceptibility is a good characterization parameter for magnetic materials, Fig. 2.1. Fig. 2.1(c) shows that in the paramagnetic region, the variation of the inverse susceptibility with temperature of a ferrite material is decidedly non-linear. Thus the ferrite materials do not obey the Curie-Weiss law, $\chi = C / (T - T_c)$ [2, 11].

2.3 Crystal Structure of Spinel Ferrites

Ferrites have the cubic structure, which is very close to that of the mineral spinel $MgO.Al_2O_3$, and are called cubic spinel. Analogous to the mineral spinel, magnetic spinel have the general formula $MeO.Fe_2O_3$ or $MeFe_2O_4$ where Me is the divalent metal ion [12]. This crystal structure was first determined by Bragg and by Nishikawa [1,11]. Formerly, spinels containing Fe were called ferrites but now the term has been broadened to include many other ferrimagnets including garnets and hexagonal ferrites these need not necessarily contain iron. The spinel lattice is composed of a close-packed oxygen (radius about 1.3Å) arrangement in which 32 oxygen ions form a unit cell that is the smallest repeating unit in the crystal network. The unit cell of the ideal spinel structures is given in Fig. 2.2. Between the layers of oxygen ions, if we simply visualize them as spheres, there are interstices that may accommodate the metal ions (radii ranging from 0.6 to 0.8Å). Now, the interstices are not all the same; some which we call A sites are surrounded by or coordinated with 4 nearest neighboring oxygen ions whose lines connecting their centers form a tetrahedron. Thus, A sites are called tetrahedral sites. The other type of sites (B sites) is coordinated by 6 nearest neighbor oxygen ions whose center connecting lines describe an octahedron. The B sites are called octahedral

sites. In the unit cell of 32 oxygen ions there are 64 tetrahedral sites and 32 octahedral sites. If all these were filled with metal ions, of either +2 or +3 valence, the positive charge would be very much greater than the negative charge and so the structure would not be electrically neutral. It turns out that of the 64 tetrahedral sites, only 8 are occupied and out of 32 octahedral sites, only 16 are occupied. Thus the unit cell contains eight formula units AB_2O_4, with 8 A sites, 16 B sites and 32 oxygen ions, and total of $8 \times 7 = 56$ ions. A spinel unit cell contains two types of subcells, Fig. 2.2. The two types of subcells alternate in a three-dimensional array so that each fully repeating unit cell requires eight subcells, Fig. 2.3
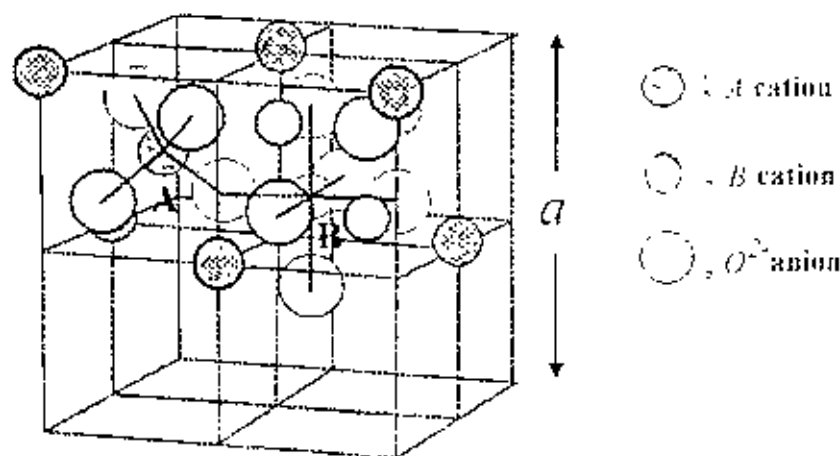
Figure 2.2. Two subcells of a unit cell of the spinel structure.
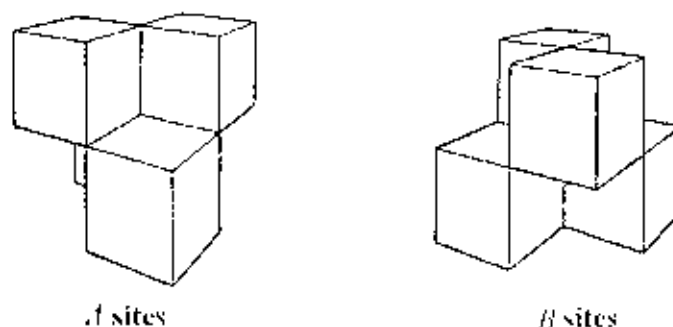
Figure 2.3. Unit cell of spinel ferrite divided into eight subcells with A and B sites

10

The positions of the ions in the spinel lattice are not perfectly regular (as the packing of hard spheres) and some distortion does occur. The tetrahedral sites are often too small for the metal ions so that the oxygen ions move slightly to accommodate them. The oxygen ions connected with the octahedral sites move in such a way as to shrink the size the octahedral cell by the same amount as the tetrahedral site expands. The movement of the tetrahedral oxygen is reflected in a quantity called the oxygen parameter, which is the distance between the oxygen ion and the face of the cube edge along the cube diagonal of the spinel subcell. This distance is theoretically equal to $3/8a_0$ where a_0 is the lattice constant [1].

2.4 Cation Distribution of Spinel Ferrites

In spinel structure the distribution of cations over the tetrahedral or A sites and octahedral or B sites can be present in a variety of ways. If all the Me^{2+} ions in $Me^{2+}Me_2^{3+}O_4$ are in tetrahedral and all Me^{3+} ions in octahedral positions, the spinel is then called normal spinel. Another cation distribution in spinel exists, where one half of the cations Me^{3+} are in the A positions and the rest, together with the Me^{2+} ions are randomly distributed among the B positions. The spinel having the latter kind of cation distribution is known as inverse spinel. The distribution of these spinels can be summarized as [2, 13-14]:

1) Normal spinels, i.e. the divalent metal ions are on A-sites: $Me^{2+}[Me_2^{3+}]O_4$,

2) Inverse spinels, i.e. the divalent metal ions are on B-sites: $Me^{3+}[Me^{2+}Me_1^{3+}]O_4$.

A completely normal or inverse spinel represents the extreme cases. Zn ferrites have normal spinel structure and its formula may be written as $Zn^{2+}[Fe^{3+}Fe^{3+}]O_4^{2-}$. On the other hand, Co ferrites have inversel spinel structure and its formula may be written as $Fe^{3+}[Co^{2+}Fe^{3+}]O_4^{2-}$. There are many spinel oxides which have cation distributions intermediate between these two extreme cases and are called mixed spinels. The general cation distribution for the spinel can be indicated as:

$$(Me_x^{2+}Me_{1-x}^{3+})[Me_{1-x}^{2+}Me_{1+x}^{3+}]O_4$$
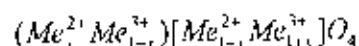
where the first and third brackets represent the A and B sites respectively. For normal spinel $x=1$, for inverse spinel $x=0$. The quantity x is a measure of the degree of

inversion. In the case of some spinel oxides x depends upon the method of preparation.

The basic magnetic properties of the ferrites are very sensitive functions of their cation distributions. Mixed ferrites having interesting and useful magnetic properties are prepared by mixing two or more different types of metal ions. The chemical formula of mixed Co-Zn ferrite may be written as $(Zn_x^{2+}Fe_{1-x}^{3+})[Co_{1-x}^{2+}Fe_{1+x}^{3+}]O_4^{2-}$ where $0 \leq x \leq 1$.

Spinel oxides are ionic compounds and hence the chemical bonding occurring in them can be taken as purely ionic to a good approximation. The total energy involved, however, consists of the Coulomb energy, the Born repulsive energy, the polarization and the magnetic interaction energy. The energy terms are all dependent on lattice constant, oxygen position parameter and the ionic distribution. In principle the equilibrium cation distribution can be calculated by minimizing the total energy with respect to these variables. But the only energy that can be written with any accuracy is the Coulomb energy. The individual preference of some ions for certain sites resulting from their electronic configuration also play an important role. The divalent ions are generally larger than the trivalent (because the larger charge produces greater electrostatic attraction and so pulls the outer orbits inward). The octahedral sites are also larger than the tetrahedral. Therefore, it would be reasonable that the trivalent ions Fe^{3+} (0.67Å) would go into the tetrahedral sites and the divalent ions Fe^{2+} (0.83Å) go into the octahedral. Two exceptions are found in Zn^{2+} and Cd^{2+} which prefer tetrahedral sites because the electronic configuration is favourable for tetrahedral bonding to the oxygen ions. Thus Zn^{2+} (0.74Å) prefer tetrahedral sites over the Fe^{3+} (0.67Å) ions. Zn^{2+} (0.74Å) and Co^{2+} (0.72Å) have almost the same ionic radius but Zn prefers tetrahedral sites and Co prefers octahedral sites because of the configuration exception. Ni^{2+} (0.78Å) and Cr^{3+} (0.64Å) have strong preferences for octahedral sites. Hence the factors influencing the distribution the cations among the two possible lattice sites are mainly their ionic radii of the specific ions, the size of the interstices, temperature, the matching of their electronic configuration to the surrounding anions and the electrostatic energy of the lattice, the so-called Madelung energy, which has the predominant contribution to the lattice energy under the constrain of overall energy minimization and charge neutrality

2.5 Interaction Between Magnetic Moments on Lattice Sites

Spontaneous magnetization of spinels (at 0K) can be estimated on the basis of their composition, cation distribution, and the relative strength of the possible interaction. Since cation-cation distances are generally large, direct (ferromagnetic) interactions are negligible. Because of the geometry of orbital involved, the strongest superexchange interaction is expected to occur between octahedral and tetrahedral cations. The strength of interaction or exchange force between the moments of the two metal ions on different sites depends on the distances between these ions and the oxygen ion that links them and also on the angle between the three ions. The nearest neighbours of a tetrahedral, an octahedral and an anion site are shown in Fig. 2.4. The interaction is greatest for an angle of 180^0 and also where the interionic distances are the shortest. Fig. 2.5 shows the interionic distances and the angles between the ions for the different type of interactions. In the A-A and B-B cases, the angles are too small or the distances between the metal ions and the oxygen ions are too large. The best combination of distances and angles are found in A-B interactions.
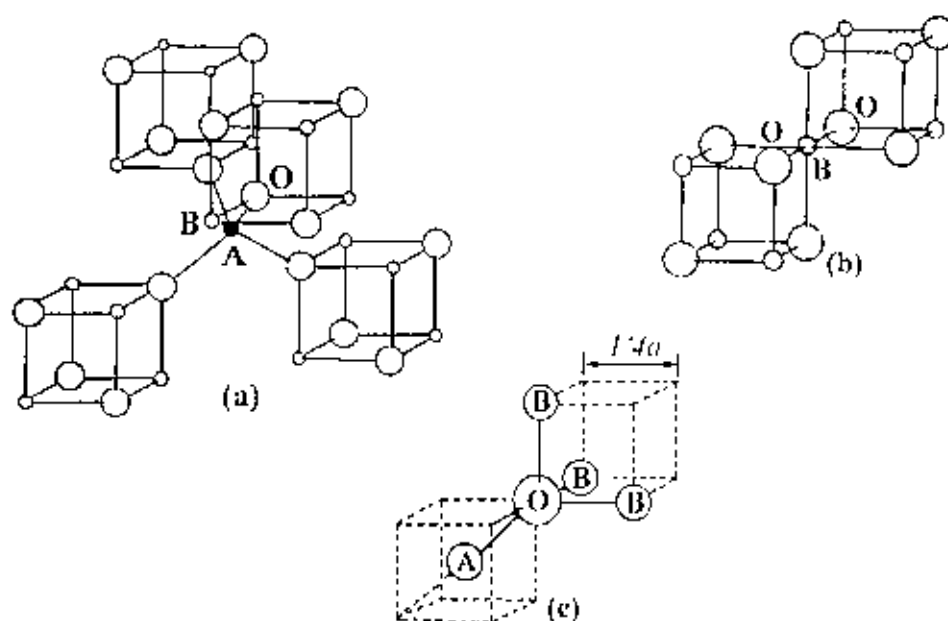
Figure 2.4. Nearest neighbours of (a) a tetrahedral site, (b) an octahedral site and (c) an anion site
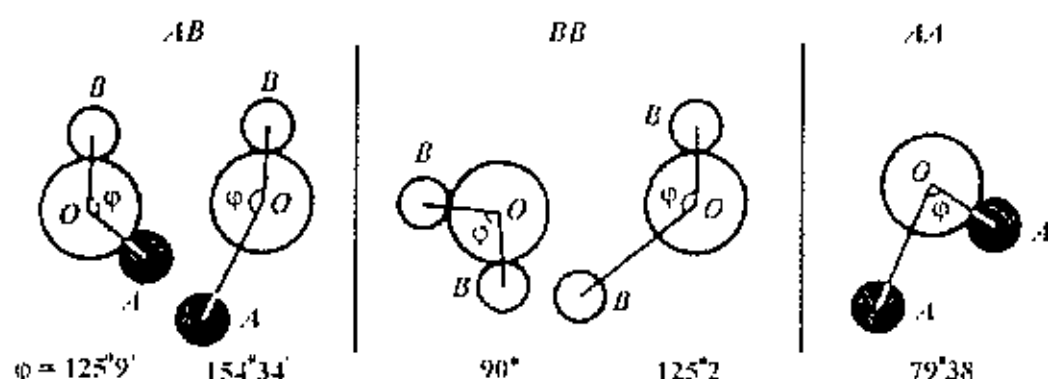
Figure 2.5. Interionic angles in the spinel structure for the different type of lattice site interactions.

For an undistorted spinel, the A-O-B angles are about 125^0 and 154^0 [1-2, 15] The B-O-B angles are 90^0 and 125^0 but the latter, one of the B-B distances is large. In the A-A case the angle is about 80^0. Therefore, the interaction between moments on the A and B site is strongest. The BB interaction is much weaker and the most unfavorable situation occurs in the AA interaction. By examining the interaction involving the major contributor, or the A-B interaction which orients the unpaired spins of these ions antiparallel. Néel was able to explain the ferrimagnetism of ferrites.

2.6 Magnetism in Spinel Ferrite

The magnetic moment of a free atom is associated with the orbital and spin motions of electrons in an incomplete sub-shell of the electronic structure of the atom. In crystals the orbital motions are quenched, that is the orbital planes may be considered to be fixed in space relative to the crystal lattice, and in such a way that in bulk the crystal has no resultant moment from this source. Moreover this orbital-lattice coupling is so strong that the application of a magnetic field has little effect upon it. The spin axes are not tightly bound to the lattice as are the orbital axes. The anions surrounding a magnetic cation subject it to a strong inhomogeneous electric field and influence the orbital angular momentum However, the spin angular momentum remains unaffected. For the first transition group elements this crystal field effect is intense partly due to the large radius of the 3d shell and partly due to the lack of any outer electronic shell to screen the 3d shell whose unpaired electrons only contribute to the magnetic moment. We have originally defined the

magnetic moment in connection with permanent magnets. The electron itself may well be called the smallest permanent magnet [1]. For an atom with a resultant spin quantum number S, the spin magnetic moment will be

$$\mu = g\sqrt{S(S+1)}\mu_B$$

where g is the Landé splitting factor and μ_B, known as the Bohr magneton, is the fundamental unit of magnetic moment. The value of g for pure spin moment is 2 and the quantum number associated with each electron spin is $\pm 1/2$. The direction of the moment is comparable to the direction of the magnetization (from South to North poles) of a permanent magnet to which the electron is equivalent. Fig. 2.6 illustrates the electronic configuration of Fe atoms and Fe^{3+} ions. Fe atom has four unpaired electrons and Fe^{3+} ion has five unpaired electrons. Each unpaired electron spin produced 1 Bohr magneton. In compounds, ions and molecules, account must be taken of the electrons used for bonding or transferred in ionization. It is the number of unpaired electrons remaining after these processes occur that gives the net magnetic moment [1]. According to the Hund's rules the moment of Fe atom and Fe^{3+} ion are $4\mu_B$ and $5\mu_B$ respectively. Similarly the moment of Fe^{2+} and Co^{2+} ion are $4\mu_B$ and $3\mu_B$ respectively.
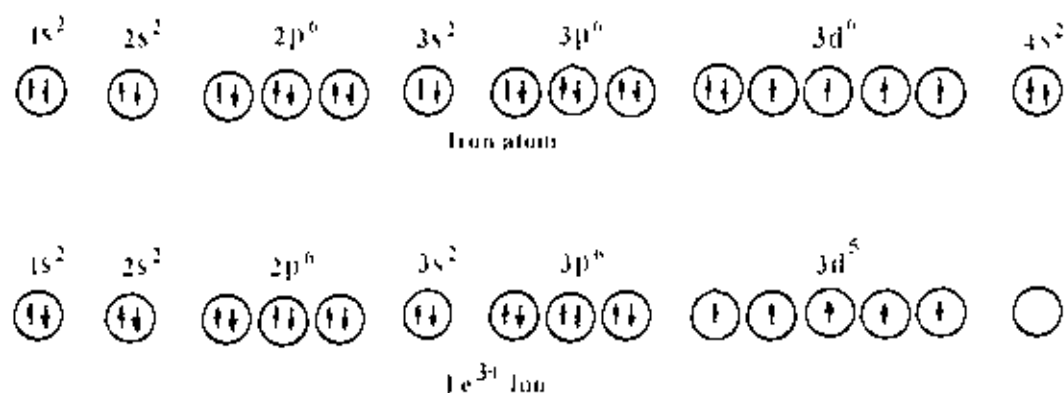
Figure 2.6. Electronic configuration of atoms and ions.

2.6.1 Exchange Interactions in Spinel

The intense short-range electrostatic field, which is responsible for the magnetic ordering, is the exchange force that is quantum mechanical in origin and is related to the overlapping of total wave functions of the neighbouring atoms. The total wave function

consists of the orbital and spin motions. Usually the net quantum number is written as S, because the magnetic moments arise mostly due to the spin motion as described above. The exchange interactions coupling the spins of a pair of electrons are proportional to the scalar product of their spin vectors [12, 14, 16],

$$V_{ij} = -2J_{ij}\,\vec{S_i}.\vec{S_j} \qquad (2.1)$$

where J_{ij} is the exchange integral given in a self explanatory notation by

$$J_{ij} = \int \psi_i^*(1)\psi_j^*(2)\left[\frac{1}{r_{12}} + \frac{1}{r_{ij}} - \frac{1}{r_{i1}} - \frac{1}{r_{j2}}\right]\psi_i(2)\psi_j(2)dv_1dv_2 \qquad (2.2)$$

In this expression r's are the distances, subscripts i and j refer to the atoms, 1 and 2 refers to the two electrons. If the J in equation (2.1) is positive, we achieve ferromagnetism. A negative J may give rise to anti-ferromagnetism or ferrimagnetism.

Magnetic interactions in spinel ferrites as well as in some ionic compounds are different from the one considered above because the cations are mutually separated by bigger anions (oxygen ions) These anions obscure the direct overlapping of the cation charge distributions, sometimes partially and some times completely making the direct exchange interaction very weak. Cations are too far apart in most oxides for a direct cation-cation interaction. Instead, superexchange interactions appear, i.e., indirect exchange via anion p-orbitals that may be strong enough to order the magnetic moments. Apart from the electronic structure of cations this type of interactions strongly depends on the geometry of arrangement of the two interacting cations and the intervening anion. Both the distance and the angles are relevant. Usually only the interactions with in first coordination sphere (when both the cations are in contact with the anion) are important. In the Néel theory of ferrimagnetism the interactions taken as effective are inter- and intra-sublattice interactions A-B, A-A and B-B. The type of magnetic order depends on their relative strength.

The superexchange mechanism between cations that operate via the intermediate anions was proposed by Kramer for such cases and was developed by Anderson and Van Vleck [13, 14]. A simple example of superexchange is provided by MnO which was chosen by Anderson. From the crystal structure of MnO it will be seen that the antiparallel manganese ions are collinear with their neighbouring oxygen ions. The O^{2-} ions each have six $2p$ electrons in three antiparallel pairs. The outer electrons of the Mn^{2+}

ions are in $3d$ sub-shells which are half filled with five electrons in each. The phenomenon of superexchange is considered to be due to an overlap between the manganese $3d$ orbits and the oxygen $2p$ orbits with a continuous interchange of electrons between them. It appears that, for the overall energy of the system to be a minimum, the moments of the manganese ions on either side of the oxygen ion must be antiparallel. The manganese magnetic moments are thus, in effect, coupled through the intervening oxygen ion. The idea is illustrated in Fig. 2.7.

In Figs. 2.7(a) and 2.7(c) the outer electrons in a pair of Mn^{2+} ions, and in an intervening O^{2-} ion in the unexcited state, are shown by the arrows. One suggested mode of coupling is indicated in Fig. 2.7(b). The two electrons of a pair in the oxygen ion are simultaneously transferred, one to the left and the other to the right. If their directions of spin are unchanged then, by Hund's rules, the moments of the two manganese ions must be antiparallel as shown. Another possibility is represented in Fig. 2.7(d). One electron only has been transferred to the manganese ion on the left. The oxygen ion now has a moment of $1\mu_B$ and if there is negative interaction between the oxygen ion and the right-hand manganese ion then again the moments of the manganese ions will be antiparallel. If these ideas are accepted then the oxygen ions play an essential part in producing antiferromagnetism in the oxide. Moreover, because of the dumbbell shape of the $2p$ orbits, the coupling mechanism should be most effective when the metal ions and the oxygen ions lie in one straight line, that is, the angle between the bonds is 180°, and this is the case with MnO.
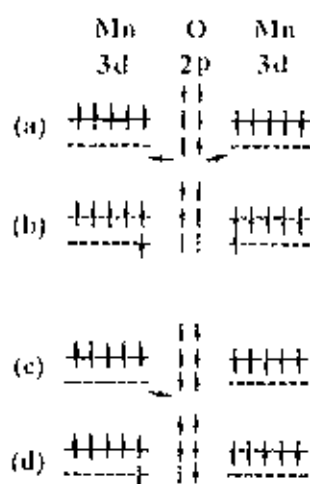
Figure 2.7. Illustrating superexchange in MnO
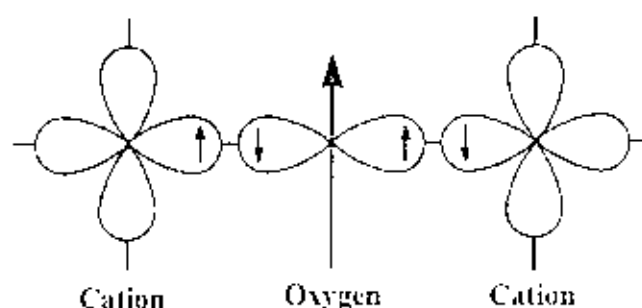
Figure 2.8. Schematic representation of the superexchange interaction in the magnetic oxides. The p orbital of an anion (center) interact with the d orbitals of the transitional metal cations

In the case of spinel ferrites the coupling is of the indirect type which involves overlapping of oxygen wave functions with those of the neighboring cations. Consider two transition metal cations separated by an O. Fig. 2.8. The O^{2-} has no net magnetic moment since it has completely filled shells, with p-type outermost orbitals. Orbital p_x has two electrons: one with spin up, and the other with spin down, consistent with pauli's exclusion principle. The essential point is that when an oxygen p orbital overlaps with a cation d orbital, one of the p electrons can be accepted by the cations. When one of the transition-metal cations is brought close the O^{2-}, partial electron overlap (between a $3d$ electron from the cation and a $2p$ electron form the O^{2-}) can occur only for antiparallel spins, because electrons with the same spin are repelled. Empty $3d$ states in the cation are available for partial occupation by the O^{2-} electron, with an antiparallel orientation. Electron overlap between the other cation and the O^{2-} then occurs resulting in antiparallel spins and therefore antiparallel order between the cations. Since the p orbitals are linear, the strongest interaction is expected to take place for $cation–O^{2-}–cation$ angles close to 180^0 [2].

2.6.2 Néel Theory of Ferrimagnetism

If we consider the simplest case of a two-sublattice system having antiparallel and non-equal magnetic moments, the inequality may be due to:

1) different elements in different sites,
2) same element in different ionic states, and

18

3) different crystalline fields leading to different effective moments for ions having the same spin.

The spins on one sublattice are under the influence of exchange forces due to the spins on the second sublattice as well as due to other spins on the same sublattice. The molecular fields acting on the two sublattices A and B can be written as [2, 11-16]

$$\vec{H}_A = \lambda_{AA}\vec{M}_A + \lambda_{AB}\vec{M}_B,$$

$$\vec{H}_B = \lambda_{AB}\vec{M}_A + \lambda_{BB}\vec{M}_B$$

where $\vec{M}_A$ and $\vec{M}_B$ are the magnetizations of the two sublattices and λ's are the Weiss constants. Since the interaction between the sublattices is antiferromagnetic, λ_{AB} must be negative, but λ_{AA} and λ_{BB} may be negative or positive depending on the crystal structure and the nature of the interacting atoms. Probably, these interactions are also negative, though they are in general quite small.

Assuming all the exchange interactions to be negative the molecular fields will be then given by

$$.\vec{H}_A = -\lambda_{AA}\vec{M}_A - \lambda_{AB}\vec{M}_B,$$

$$\vec{H}_B = -\lambda_{AB}\vec{M}_A - \lambda_{BB}\vec{M}_B$$

Since in general, λ_{AA} and λ_{BB} are small compared to λ_{AB}, it is convenient to express the strengths of these interactions relative to the dominant λ_{AB} interaction.

Let $\qquad\qquad \lambda_{AA} = \alpha\lambda_{AB}$

and $\qquad\qquad \lambda_{BB} = \beta\lambda_{AB}$

In an external applied field $\vec{H}$, the fields acting on A and B sites are

$$\vec{H}_A = \vec{H} - \lambda_{AB}(\alpha\vec{M}_A - \vec{M}_B),$$

$$\vec{H}_B = \vec{H} - \lambda_{AB}(\vec{M}_A - \beta\vec{M}_B)$$

At temperatures higher than the transition temperature, T_N, $\vec{H}_A$, $\vec{M}_A$ and $\vec{M}_B$ are all parallel and we can write

$$\vec{M}_A = \frac{C_A}{T}[\vec{H} - \lambda_{AB}(\alpha\vec{M}_A - \vec{M}_B)], \qquad\qquad (2.3)$$

$$\vec{M}_B = \frac{C_B}{T}[\vec{H} - \lambda_{AB}(\vec{M}_A - \beta\vec{M}_B)] \tag{2.4}$$

where C_A and C_B are the Curie constants for the two sublattices.

$$C_A = N_A g\mu_B^2 S_A (S_A + 1)/3K$$

and $\qquad\qquad C_B = N_B g\mu_B^2 S_B (S_B + 1)/3K$

N_A and N_B denote the number of magnetic ions on A and B sites respectively and S_A and S_B are their spin quantum numbers. Solving for the susceptibility. χ, one gets [2, 11]

$$\frac{1}{\chi} = \frac{T}{C} - \frac{1}{\chi_0} - \frac{b}{T-\theta}$$

$$\frac{1}{\chi} = \frac{T + (C/\chi_0)}{C} - \frac{b}{T-\theta} \tag{2.5}$$

where C, χ_0, b and θ are constants for particular substance and are given by

$$C = C_A + C_B$$

$$\frac{1}{\chi_0} = -\frac{1}{C^2}[C_A^2\lambda_{AA} + C_B^2\lambda_{BB} + 2C_A C_B\lambda_{AB}]$$

$$b = \frac{C_A C_B}{C^3}[C_A^2(\lambda_{AA} - \lambda_{BB})^2 + C_B^2(\lambda_{BB} - \lambda_{AB})^2$$

$$- 2C_A C_B\{\lambda_{AB}^2 - (\lambda_{AA} + \lambda_{BB})\lambda_{AB} + \lambda_{AA}\lambda_{BB}\}]$$

$$\theta = -\frac{C_A C_B}{C}(\lambda_{AB} + \lambda_{BB}) - 2\lambda_{AB}$$

Equation (2.5) represents a hyperbola, and the physically meaning part of it is plotted in Fig. 2.9. This curvature of the plot of $1/\chi$ versus T is a characteristics feature of a ferrimagnet. It cuts the temperature axis at T_c, called the Ferrimagnetic Curie point. At high temperatures the last term of equation (2.5) become negligible, and reduces to a Curie-Weiss law:

$$\chi = \frac{C}{T + (C/\chi_0)}$$

This is the equation of straight line, shown dashed in Fig 2.9. to which the $1/\chi$ versus T curve becomes asymptotic at high temperatures.

20
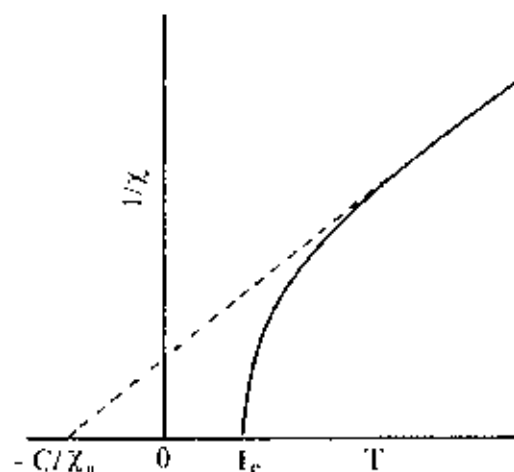
Figure 2.9. The temperature dependence of the inverse susceptibility for ferrimagnets.

The Ferrimagnetic Curie temperature T_c is obtained from equations (2.3) and (2.4) with $H = 0$ and setting the determinant of the coefficients of M_i equal to zero. This gives

$$T_c = \frac{1}{2}[C_A\lambda_{AA} + C_B\lambda_{BB} + \{(C_A\lambda_{AA} - C_B\lambda_{BB})^2 + 4C_A C_B\lambda_{AB}^2\}^2] \qquad (2.6)$$

Equation (2.5) is in good agreement with the experiment, except near the Curie point. The experimental Curie temperature, the temperature at which the susceptibility becomes infinite and spontaneous magnetization appears, is lower than the theoretical Curie temperature [11]. This disagreement between theory and experiment in the region of Curie point is presumably due to the short-range spin order (spin clusters) at temperatures above experimental T_c [2, 11].
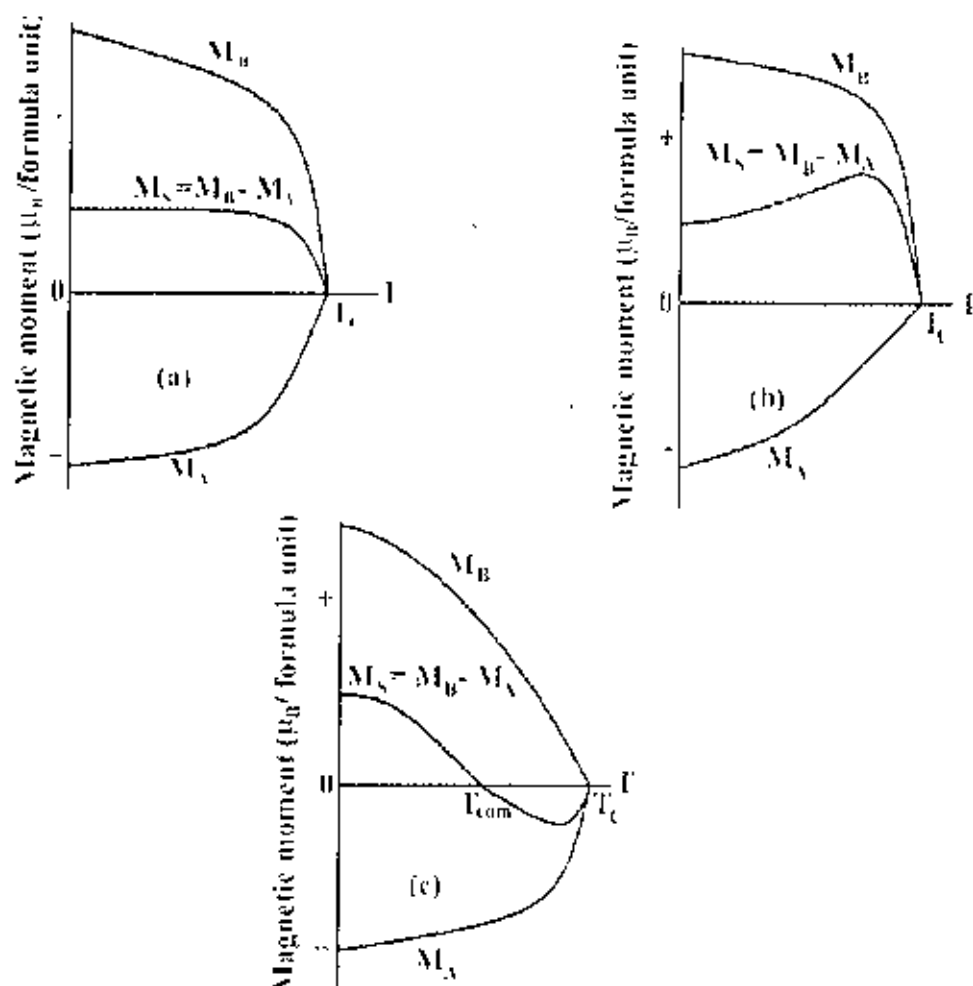
Figure 2.10. Superposition of various combinations of two opposing sublattice magnetizations producing differing resultants including one with a compensation point (schematic).

The sublattice magnetizations will in general have different temperature dependences because the effective molecular fields acting on them are different. This suggests the possibility of having anomaly in the net magnetization versus temperature curves, Fig. 2.10. For most ferrimagnets the curve is similar to that of ferromagnets, but in a few cases there be a compensation point in the curve, Fig. 2.10(c) [1, 11]. At a point below the Curie temperature point, the two sublattice magnetizations are equal and thus appear to have no moment. This temperature is called the compensation point. Below this temperature one sublattice magnetization is larger and provides the net moment. Above this temperature the other magnetization does dominates and the net magnetization reverses direction.

22

The essential requisite for Neel configuration is a strong negative exchange interaction between A and B sublattices which results in their being magnetized in opposite directions below the transition point. But there may be cases where intrasublattice interactions are comparable with intersublattice interaction. Neel's theory predicts paramagnetism for such substances at all temperatures. This is unreasonable since strong AA or BB interaction may lead to some kind of ordering especially at low temperature. In the cases of no AB interaction, antiferromagnetic ordering may be expected either in the A or in the B sublattice. Under certain conditions there may be non-collinear spin arrays of still lower energy.

2.6.3 Effect of Zinc Substitution on the Magnetic Moments in Spinel Ferrites

Fe_3O_4 has ferromagnetic properties because of its inverse structure which leads to the formation of domains. A unit cell of Fe_3O_4 contains eight formula units each of which may be written in the form $Fe^{3+}[Fe^{2+}Fe^{3+}]O_4^{2-}$ [13]. Snoek and his co-workers found that oxides of inverse structure could be artificially produced in which the divalent ions of another element, for example Mn, Ni, Co, Mg or Cu, could be substituted for the divalent Fe^{2+} ions in Fe_3O_4. An extensive range of ferrites could thus be made having the general formula $\overrightarrow{Fe^{3+}}[\overset{\cdot\cdot}{M^{2+}}\overset{\cdot\cdot}{Fe^{3+}}]O_4^{2-}$, where arrows indicate spin ordering. Since the trivalent iron ions are equally distributed on A and B sites they cancel each other out magnetically, and the magnetic moment per formula unit is then theoretically the same as the magnetic moment of the divalent ion. The Co ferrite has a moment of $3.3\mu_B$ compared with a theoretical value of $3\mu_B$ [1]. Zn ferrite is a normal spinel, with Zn^{2+} $(3d^{10})$ ions in A sites have zero magnetic moment, Fe^{3+} ions in B sites have a magnetic moment $5\mu_B$. The cation distribution can be written as $Zn^{2+}[\overrightarrow{Fe^{3+}}\overleftarrow{Fe^{3+}}]O_4$, where spin ordering is indicated by arrows. The zero magnetic moment of Zn^{2+} ions leaves trivalent iron ions on B sites with a negative BB interaction between equal ions. Therefore Zn ferrite is not ferromagnetic. Zinc ferrite therefore be expected to be antiferromagnetic and thus to have a Néel point, though measurements show it to be paramagnetic only [1-2, 11, 13].

23

Magnetic properties can be modified widely by cation substitution. An illustrative case is substituion of Co by Zn in Co ferrite to form solid solutions $Co_{1-x}Zn_xFe_2O_4$. The cation distribution can be written as $(Zn_x^{2+}Fe_{1-x}^{3+})[Co_{1-x}^{2+}Fe_{1+x}^{3+}]O_4^{2-}$ [2]. Zn^{2+} is diamagnetic and its main effect is to break linkages between magnetic cations. Another effect is to increase interaction distance by expanding the unit cell, since it has an ionic radious larger than the Co and Fe radii. The most remarkable effect is that substitution of this diamagnetic cation (Zn) results in a significant increase in magnetic moment in a number of spinel solid solutions, Fig. 2.11. Magnetic moment as a function of Zn content shows an increase for small substitutions, goes through a maximum for intermediate values, decreases and finally vanishes for high Zn contents.
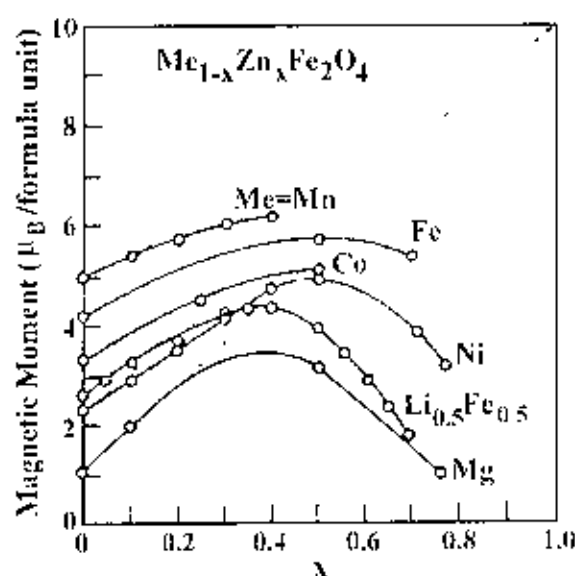
Figure 2.11. Variation of Magnetic moment (in Bohr magnetons per formula unit) with increasing zinc substitution [1, 2].

A simple analysis shows that this increase can be expected for an antiparallel alignment. As the Zn content increases, magnetic moments decreases in sublattice A and increase in sublattice B. If the magnetic moment of Fe^{3+} and Co^{2+} are 5 and ~3.3 μ_B/ion, respectively, then, per formula unit, the total moment in Bohr magnetons on B sublattice is $3.3(1-x)+5(1+x)$ and on A sublattice the total antiparallel moment is $5(1-x)$. If the resultant moment per formula unit is $M_s(0)$, then by taking the difference of A and B moments [13],

$$M_S(0) = 3.3(1 - x) + 5(1 + x) - 5(1 - x)$$

$$= x(10 - 3.3) + 3.3$$

A linear relationship is obtained with a slope of 6.7, predicting a moment value of $10\mu_B$ per formula unit for Zn substitution $x = 1$, as shown by the broken lines in Fig. 2.11. This relationship is not followed over the entire composition range. However, as the Zn content increases, $A - O - B$ interactions become too weak and $B - O - B$ interactions begin to dominate. That is, the average distance between the interacting spins gets larger. As a consequence, the system becomes frustrated causing a perturbation to the magnetically ordered spins as large number of B sites spins gets non-magnetic impurity atoms as their nearest neighbors.

(a)   (b)   (c)
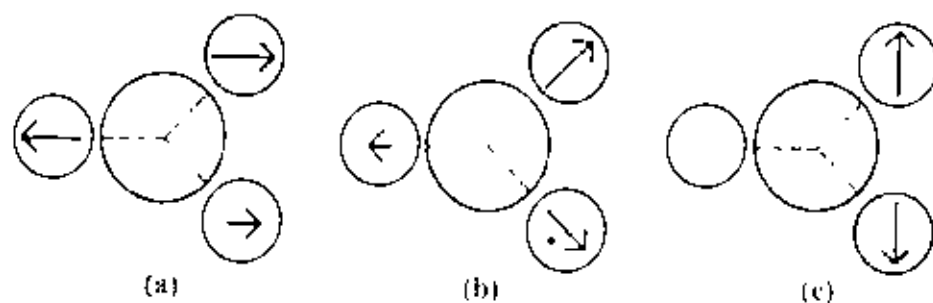
Figure 2.12. Schematic representation of spin arrangements in $Co_{1-x}Zn_xFe_2O_4$ (a) ferrimagnetic (for $x \leq 0.5$), (b) triangular or Yafet-Kittel (for $x > 0.5$), and (c) antiferromagnetic for $x \approx 1$.

The B spins are no longer held in place due to this weak anti-ferromagnetic A-B interaction leading to non-collinearity or canting among the B sublattice. Thus for $x > 0.5$ Zn content, instead of a collinear antiparallel alignment, canted structure appears, where spins in B sites are no longer parallel [2, 17], Fig. 2.12. Evidence of this triangular structure has been observed by neutron diffraction [18]; a theoretical analysis showed that departure from collinear order depends on the ratio of the $A - O - B$ to $B - O - B$ molecular field coefficients, $\lambda_{AB} / \lambda_{BB}$ [19]. For high Zn concentration, $B - O - B$ interactions dominant and the ferrite become antiferromagnetic for $x = 1$ [2].

2.7 Microstructure of Polycrystalline Materials

A polycrystal is much more than many tiny crystals bonded together. The interfaces between the crystals, or the *grain boundaries* which separate and bond the grains, are complex and interactive interfaces. The whole set of a given material's properties (mechanical, chemical and especially electrical and magnetic) depend strongly on the nature of the microstructure.

In the simplest case, the grain boundary is the region, which accommodates the difference in crystallographic orientation between the neighbouring grains. For certain simple arrangements, the grain boundary is made of an array of dislocations whose number and spacing depends on the angular deviation between the grains. The ionic nature of ferrites leads to dislocation patterns considerably more complex than in metals, since electrostatic energy accounts for a significant fraction of the total boundary energy [2].

For low-loss ferrite, Ghate [1] states that the grain boundaries influence properties by

1) creating a high ressistivity intergranular layer.
2) acting as a sink for impurities which may act as a sintering aid and grain growth modifiers.
3) providing a path for oxygen diffusion, which may modify the oxidation state of cations near the boundaries.

In addition to grain boundaries, ceramic imperfections can impede domain wall motion and thus reduce the magnetic property. Among these are pores, cracks, inclusions, second phases, as well as residual strains. Imperfections also act as energy wells that pin the domain walls and require higher activation energy to detach. Stresses are microstructural imperfections that can result from impurities or processing problems such as too rapid a cool. They affect the domain dynamics and are responsible for a much greater share of the degradation of properties than would expect [1].

Grain growth kinetics depends strongly on the impurity content. A minor dopant can drastically change the nature and concentration of defects in the matrix, affecting grain boundary motion, pore mobility and pore removal [2, 20]. The effect of a given

dopant depends on its valence and solubility with respect to host material. If it is not soluble at the sintering temperature, the dopant becomes a second phase which usually segregates to the grain boundary.
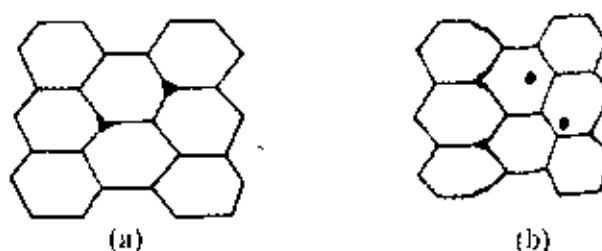
Figure 2.13. Porosity character. (a) intergranular, (b) intragranular.

The porosity of ceramic samples results from two sources, intragranular porosity and intergranular porosity, Fig. 2.13. An undesirable effect in ceramic samples is the formation of exaggerated or discontinuous grain growth which is characterized by the excessive growth of some grains at the expense of small, neighbouring ones, Fig. 2.14. When this occurs, the large grain has a high defect concentration. Discontinuous growth is believed to result from one or several of the following: powder mixtures with impurities; a very large distribution of initial particle size; sintering at excessively high temperatures; in ferrites containing *Zn* and /or *Mn*, a low O_2 partial pressure in the sintering atmosphere. When a very large grain is surrounded by smaller ones, it is called 'duplex' microstructure.

Figure 2.14. Grain growth (a) discontinuous, (b) duplex (schematic).

2.8 Theories of Permeability

Permeability is defined as the proportionality constant between the magnetic field induction B and applied field intensity H [2, 15, 21]

$$B = \mu H \tag{2.7}$$

If the applied field is very low, approaching zero, the ratio will be called the initial permeability, Fig. 2.15 and is given by

$$\mu_i = \frac{\Delta B}{\Delta H}_{(\Delta H \to 0)}$$

This simple definition needs further sophistications. A magnetic material subjected to an ac magnetic field can be written as

$$H = H_0 e^{i\omega t} \tag{2.8}$$

It is observed that the magnetic flux density B lag behind H. This is caused due to the presence of various losses and is thus expressed as

$$B = B_0 e^{i(\omega t - \delta)} \tag{2.9}$$

Here δ is the phase angle that marks the delay of B with respect to H. The permeability is then given by

$$\mu = \frac{B}{H} = \frac{B_0 e^{i(\omega t - \delta)}}{H_0 e^{i\omega t}} = \frac{B_0 e^{-i\delta}}{H_0} = \frac{B_0}{H_0} \cos\delta - i\frac{B_0}{H_0}\sin\delta = \mu' - i\mu'' \tag{2.10}$$

where

$$\mu' = \frac{B_0}{H_0}\cos\delta \tag{2.11}$$

and

$$\mu'' = \frac{B_0}{H_0}\sin\delta \tag{2.12}$$

The real part (μ') of complex permeability (μ), as expressed in equation (2.10) represents the component of B which is in phase with H, so it corresponds to the normal permeability. If there are no losses, we should have $\mu = \mu'$. The imaginary part μ'' corresponds to that of B, which is delayed by phase angle 90^0 from H [11, 15]. The presence of such a component requires a supply of energy to maintain the alternating magnetization, regardless of the origin of delay. The ratio of μ'' to μ', as is evident from equation (2.12) and (2.11) gives

$$\frac{\mu''}{\mu'} = \frac{\dfrac{B_0}{H_0}\sin\delta}{\dfrac{B_0}{H_0}\cos\delta} = \tan\delta \tag{2.13}$$

This $\tan\delta$ is called loss factor.

The quality factor is defined as the reciprocal of this loss factor, i.e.

$$\text{Quality factor} = \frac{1}{\tan\delta} \tag{2.14}$$

And the relative quality factor, $Q = \dfrac{\mu'}{\tan\delta}$ $\tag{2.15}$
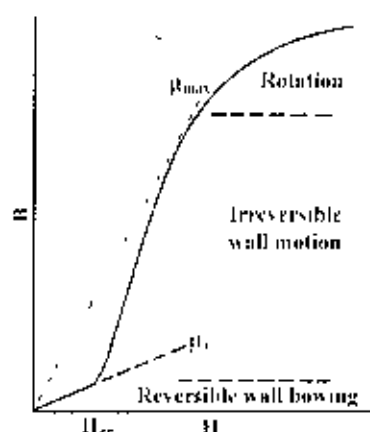
Figure 2.15. Schematic magnetization curve showing the important parameters: initial permeability, μ_i (the slope of the curve at low fields) and the main magnetization mechanism in each magnetization range.

The curves that show the variation of both μ' and μ'' with frequency are called the magnetic spectrum or permeability spectrum of the material [11]. The variation of permeability with frequency is referred to as dispersion. The measurement of complex permeability gives us valuable information about the nature of domain wall and their movements. In dynamic measurements the eddy current loss is very important. This occurs due to the irreversible domain wall movements. The permeability of a ferrimagnetic substance is the combined effect of the wall permeability and rotational permeability mechanisms.

2.8.1 Mechanisms of Permeability

The mechanisms can be explained as follows: A demagnetized magnetic material is divided into number of Weiss domains separated by Bloch walls. In each domain all the magnetic moments are oriented in parallel and the magnetization has its saturation value M_s. In the walls the magnetization direction changes gradually from the direction of magnetization in one domain to that in the next. The equilibrium positions of the walls result from the interactions with the magnetization in neighboring domains and from the influence of pores; crystal boundaries and chemical inhomogeneities which tend to favour certain wall positions.

2.8.1.1 Wall Permeability

The mechanism of wall permeability arises from the displacement of the domain walls in small fields. Lets us consider a piece of material in the demagnetized state, divided into Weiss domains with equal thickness L by means of 180° Bloch walls (as in the Fig. 2.16). The walls are parallel to the YZ plane. The magnetization M_s in the domains is oriented alternately in the $+Z$ or $-Z$ direction. When a field H with a component in the $+Z$ direction is applied, the magnetization in this direction will be favoured. A displacement dx of the walls in the direction shown by the dotted lines will decrease the energy density by an amount [22, 23]:

$$\frac{2M_sH_zdx}{L}$$

This can be described as a pressure M_sH_z exerted on each wall. The pressure will be counteracted by restoring forces which for small deviations may assume to be kdx per unit wall surface. The new equilibrium position is then given by

$$d = \frac{M_sH_zdx}{L}$$

From the change in the magnetization

$$\Delta M = \frac{2M_sd}{L},$$

30

the wall susceptibility χ_w may be calculated. Let H makes the angle θ with Z direction. The magnetization in the θ direction becomes

$$(\Delta M)_\theta = \frac{2M_s d}{L}\cos\theta . \text{ And with } H_z = H\cos\theta \text{ and } d = \frac{2M_s H_z}{K}$$

We obtain

$$\chi_w = \frac{(\Delta M)_\theta}{H} = \frac{4M_s^2 \cos^2 \theta}{KL} \tag{2.16}$$
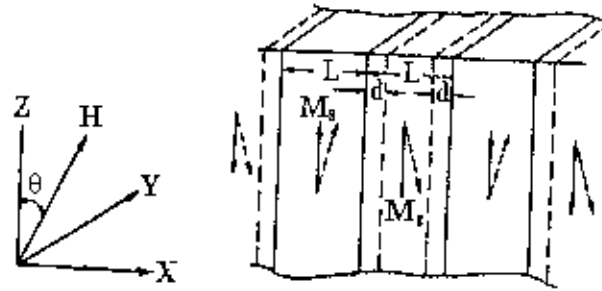
Figure 2.16. Magnetization by wall motion and spin rotation

2.8.1.2 Rotational Permeability

The rotational permeability mechanism arises from rotation of the magnetization in each domain. The direction of M can be found by minimizing the magnetic energy E as a function of the orientation. Major contribution to E comes from the crystal anisotropy energy. Other contributions may be due to the stress and shape anisotropy. The stress may influence the magnetic energy via the magnetostriction. The shape anisotropy is caused by the boundaries of the sample as well as by pores, nonmagnetic inclusions and inhomogeneities. For small angular deviations, α_x and α_y may be written as

$$\alpha_x = \frac{M_x}{M_y} \text{ and } \alpha_y = \frac{M_y}{M_x} .$$

For equilibrium Z-direction, E may be expressed as [22]

$$E = E_0 + \frac{1}{2}\alpha_x^2 E_{xx} + \frac{1}{2}\alpha_y^2 E_{yy}$$

31

where it is assumed that x and y are the principal axes of the energy minimum. Instead of E_{xx} & E_{yy}, the anisotropy field H_x^A and H_y^A are often introduced. Their magnitude is given by

$$H_y^A = \frac{E_{xx}}{2M_s} \text{ and } H_x^A = \frac{E_{yy}}{2M_s}.$$

H_x^A & H_y^A represent the stiffness with which the magnetization is bound to the equilibrium direction for deviations in the x and y direction, respectively. The rotational susceptibilities $\chi_{r,x}$ and $\chi_{r,y}$ for fields applied along x and y directions, respectively are

$$\chi_{r,x} = \frac{M_s}{H_x^A} \text{ and } \chi_{r,y} = \frac{M_s}{H_y^A}.$$

For cubic materials it is often found that H_x^A and H_y^A are equal. For $H_x^A = H_y^A = H^A$ and a field H which makes an angle θ with the Z direction (as shown in Fig. 2.16) the rotational susceptibility, $\chi_{r,x}$ in one crystallite becomes

$$\chi_{r,c} = \frac{M_s}{H^A} \sin^2 \theta \tag{2.17}$$

A polycrystalline material consisting of a large number of randomly oriented grains of different shapes, with each grain divided into domains in a certain way. The rotational susceptibility χ_r of the material has to be obtained as a weighted average of $\chi_{r,c}$ of each crystallite, where the mutual influence of neighbouring crystallites has to be taken into account. If the crystal anisotropy dominates other anisotropies, then H^A will be constant throughout the material, so only the factor $\sin^2 \theta$ (equation 2.17) has to be averaged. Snoek [23] assuming a linear averaging of $\chi_{r,c}$ and found

$$\chi_r = \frac{2M_s}{3H^A}$$

The total internal susceptibility

$$\chi = \chi_w + \chi_r = \frac{4M_s^2 \cos^2 \theta}{KL} + \frac{2M_s}{3H^A} \tag{2.18}$$

If the shape and stress anisotropies cannot be neglected, H^d will be larger. Any estimate of χ_r will then be rather uncertain as long as the domain structure, and the pore distribution in the material are not known. A similar estimate of $\chi_\shortparallel$ would require knowledge of the stiffness parameter k and the domain width L. These parameters are influenced by such factors as imperfection, porosity and crystallite shape and distribution which are essentially unknown.

References

[1]   A. Goldman, *Handbook of Modern Ferromagnetic Materials*, Kulwer Acad. Pub. Boston, U.S.A (1999).

[2]   R. Valenzuela, *Magnetic Ceramics*, Cambridge University Press, Cambridge (1994)

[3]   M. M. Haque, "Influence of additives on the magnetic and electrical properties of iron-excess Mn-Zn ferrites," *M. Phil. Thesis*, BUET, Bangladesh (2000).

[4]   J. Tasaki and T. Ito, *Intl. Conf. On Ferrite*, Japan, 1970.

[5]   T. Nakamura, "Low-temperature sintering of Ni-Zn-Cu ferrite and its permeability spectra," *Journal of Magnetism and Magnetic Materials*, **168**, 285 (1997).

[6]   E. Roess, *Ferrites*, U. of Tokyo Press, Tokyo, 187 (1971)

[7]   N. Rezlescu, E. Rezlescu, C. Pasnicu and M. L. Craus, "Effects of the rare-earth ions on some properties of a Nickel-Zinc ferrite," *J. Phys.: Condens. Matter*, **6**, 5707 (1994).

[8]   E. Rezlescu, L. Sachelarie, P. D. Popa and N. Rezlescu "Effect of substitution of divalent ions on the electrical and magnetic properties of Ni-Zn-Me ferrites, *IEEE Transactions on Magnetics*, **36**, 3962 (2000)

[9]   A. Globus, *2nd EES Conf. on Soft Magnetic Materials*, Wolfson Center for Magnetic Technology, Cardiff, Wales, (1975)

[10]   M. A. Ahmed and M. A. El Hiti, "Electrical and dielectric properties of $Zn_{0.80}Co_{0.20}Fe_2O_4$," *J. Phys. III France* **5**, 775(1995)

[11]   B. D. Cullity, *Introduction to Magnetic Materials*, Addison-Wisley Publishing Company, Inc., California (1972).

[12]   M. A. Wahab, *Solid State Physics Structure and Properties of Materials*, Narosa Publishing House, New Delhi (1999).

[13]   F. Brailsford, *Physical Principles of Magnetism*, D. Van Nostrand Company Ltd., London (1966).

[14]   A. J. Dekker, *Solid State Physics*, Macmillan India Ltd., New Delhi (1998).

[15]   S. Chikazumi, *Physics of Magnetism*, Jhon Wiley & Sons, Inc., New York (1966).

[16]   C. Kittel, *Introduction to Solid State Physics*, 7th edition, Jhon Wiley & Sons, Inc., Singapore (1996).

[17]   A. K. M. Akther Hossain, M. Seki, T. Kawai and H. Tabata, "Colossal magnetoresistance in spinel type $Zn_{1-x}Ni_xFe_2O_4$," *J. Appl. Phys.*, **96**, 1273 (2004).

[18]   N. S. Satya Murthy, M. G. Natera and S. I. Youssef, "Yafet-Kittel angles in nickel-zinc ferrites," *Physical Review*, **181**, 969 (1969).

[19]   Y. Yafet and C. Kittel, "Antiferromagnetic arrangements in ferrites," *Physical Review*, **87**, 290 (1952).

[20]   M. F. Yan and D. W. Johnson, "Impurity induced exaggerated grain growth in Mn-Zn ferrites," *J. Am. Ceram. Soc.*, **61**, 342 (1978).

[21]   D. Hadfield, *Permanent Magnets and Magnetism*, Jhon Wiley & Sons, Inc., New York (1962).

[22]   S. S. Sikder, "Temperature dependence of magnetization and induced magnetic anisotropy of some Fe, Co and Ni-based amorphous ribbons, *Ph. D. Thesis*, BUET, Bangladesh (1999)

[23]   J. L. Snoek, "Dispersion and absorptions in magnetic ferrites at frequencies above Mc/s," *Physica*, **14**, 207 (1948).

CHAPTER 3
SAMPLE PREPARATION AND STRUCTURAL CHARACTERIZATION

3.1 Introduction

A goal common to all the ferrites is the formation of the spinel structure. Now a days, the majority of ferrite powders are made by the conventional Ceramic process or Solid State Reaction technique. Most of the non-conventional processes are involved in producing the powder by a wet method. Among these methods, some are [1,2]:

1) Co-precipitation
2) Organic precursors
3) Sol-gel synthesis
4) Spray-drying
5) Freeze-drying
6) Combustion synthesis
7) Glass crystallization

In this chapter, we describe the solid state reaction method that is used in this research work.

3.2 Conventional Solid State Reaction Method

In the solid state reaction method, the required composition is usually prepared form the appropriate amount of raw mineral oxides or carbonates by crushing, grinding and milling. The most common type of mill is the ball mill, which consists of a lined pot with hard spheres or rod inside. Milling can be carried out in a wet medium to increase the degree of mixing. This method depends on the solid state inter-diffusion between the raw materials. Solids do not usually react at room temperature over normal time scales. Thus it is necessary to heat them at higher temperatures for the diffusion length $(2Dt)^{1/2}$ to exceed the particle size, where D is the diffusion constant for the fast-diffusing species, and t is the firing time. The ground powders are then calcined in air

or oxygen at a temperature above $1000\degree C$. For some time, this process is continued until the mixture is converted into the correct crystalline phase. The calcined powders are again crushed into fine powders. The pellets or toroid shaped samples are prepared from these calcined powders using die-punch assembly or hydrostatic or isostatic pressure. Sintering is carried out in the solid state, at temperature ranging $1100\text{-}1400\degree C$, for times of typically 1-40 h and in various atmospheres (e.g. Air, O_2 and N_2) [3-6]. Fig. 3.1 shows, diagrammatically, the stages followed in ferrite preparation.

The general solid state reaction leading to a ferrite $MeFe_2O_4$ may be represented as

$$MeO + Fe_2O_3 \longrightarrow MeFe_2O_4$$
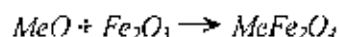
where *Me* is the divalent ions. There are basically four steps in the preparation of ferrite.

1) Preparation of materials to form an intimate mixture with the metal ions in the ratio which they will have in the final product.

2) Heating of this mixture to form the ferrite (often called calcining).

3) Grinding the calcined powders and pressing the fine powders into the required shape, and

4) Sintering to produce a highly densified product.

3.3 Details of Calcining, Pressing and Sintering

Calcining is defined as the process of obtaining a homogeneous and phase pure composition of mixed powders by heating them for a certain time at a high temperature and then allowing it to cool slowly. During the calcining stage, the reaction of Fe_2O_3 with metal oxide (say, MeO or Me'_2O_3) takes place in the solid state to form spinel according to the reactions [7]:

$$MeO + Fe_2O_2 \longrightarrow MeFe_2O_4 \text{ (Spinel)}$$

$$2Me'_2O_3 + 4Fe_2O_3 \longrightarrow 4Me'Fe_2O_4 \text{ (Spinel)} + O_2$$
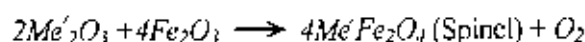
The CoO creeps into Fe_2O_3 as below, to form an intermediate phase $CoFe_2O_4$ at low temperature

$$Fe_2O_3 + CoO \longrightarrow CoFe_2O_4$$
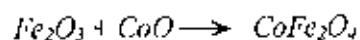
After that Zn ions are introduced by

$$(1-x)CoFe_2O_4 + xZnO + xFe_2O_3 \longrightarrow Co_{1-x}Zn_xFe_2O_4$$

Oxides of raw materials

↓

Weighing by different mole percentage

↓

Dry mixing by agate mortar

↓

Wet mixing by ball milling

↓

Drying

↓

Calcining

↓

Milling and adding binder

↓

Pressing to desired shapes

↓

Sintering

↓

Finished products
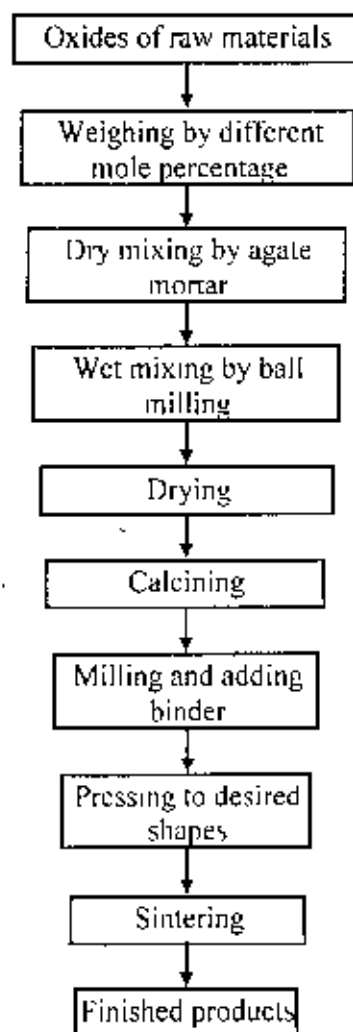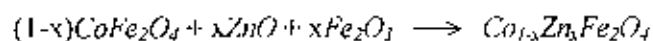
Figure 3.1. Flow chart of the stages in preparation of spinel ferrite.

The calcining process can be repeated several times to obtain a high degree of homogeneity. The calcined powders are crushed into fine powders. The ideal characteristics of fine powders are [2]:

1) small particle size (sub micron)
2) narrow distribution in particle size
3) dispersed particles
4) equiaxed shape of particles
5) high purity
6) homogeneous composition.

A small particle size of the reactant powders provides a high contact surface area for initiation of the solid state reaction, diffusion paths are shorted, leading to more efficient completion of the reaction. Porosity is easily eliminated if the initial pores are very small. A narrow size distribution of spherical particles as well as a dispersed state is important for compaction of the powder during green-body formation. Grain growth during sintering can be better controlled if the initial size is small and uniform.

A binder is usually added prior to compaction, at a concentration lower than 5wt % [2]. Binders are polymers or waxes; the most commonly used binder in ferrite is polyvinyl alcohol. The binder facilitates the particles flow during compacting and increases the bonding between the particles, presumably by forming bonds of the type *particle-binder-particle*. During sintering, binders decompose and are eliminated from the ferrite. Pressures are used for compacting very widely but are commonly several tons per square inch (i. e., up to $10^8 \, N \, m^{-2}$).

Sintering is defined as the process of obtaining a dense, tough body by heating a compacted powder for a certain time at a temperature high enough to significantly promote diffusion, but clearly lower than the melting point of the main component. The driving force for sintering is the reduction in surface free energy of the powder. Part of this energy is transferred into interfacial energy (grain boundaries) in the resulting polycrystalline body [2, 8]. The sintering time, temperature and the furnace atmosphere play very important role on the magnetic property of ferrite materials. The purposes of sintering process are:

1) to bind the particles together so as to impart sufficient strength to the product,

2) to densify the material by eliminating the pores and

3) to homogenize the materials by completing the reactions left unfinished in the calcining step.

Sintering of crystalline solids is dealt by Coble and Burke [9] who found the following empirical relationship regarding rate of grain growth:

$$\bar{d} = k t^n$$

where $\bar{d}$ is the mean grain diameter, n is about $1/3$, t is sintering time and k is a temperature dependent parameter. Sintering is divided into three stages, Fig. 3.2 [2, 10].

Stage 1. Contact area between particles increases,

Stage 2. Porosity changes from open to closed porosity,

Stage 3. Pore volume decreases; grains grow.
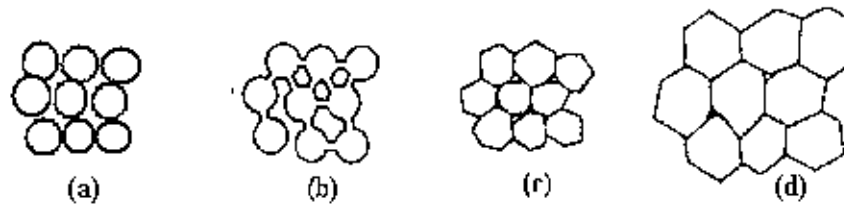
Figure 3.2. Schematic representation of sintering stages. (a) greenbody, (b) initial stage. (c) intermediate stage, and (d) final stage.

In the initial stage, neighbouring particles form a neck by surface diffusion and presumably also at high temperatures by an evaporation-condensation mechanism. Grain growth begins during the intermediate stage of sintering. Since grain boundaries are the sinks for vacancies, grain growth tends to decrease the pore elimination rate due to the increase in distance between pores and grain boundaries, and by decreasing the total grain boundary surface area. In the final stage, the grain growth is considerably enhanced and the remaining pores may become isolated.

In *Co-Zn* ferrites, the presence of *Zn* complicates the sintering process because high temperature coupled with low oxygen firing will cause *Zn* loss. High density is important for high permeability, but so is *Zn* conservation. Tasaki [1] described two alternative firings to achieve high density:

1) Low sintering temperature excluding O_2 (Vacuum, argon, nitrogen),

2) High temperature in pure oxygen to reduce Zn loss.

Accordingly, other properties correlated along with density:

1) Lattice constant is greater for O_2, smaller for vacuum

2) Curie temperature is greater for vacuum, smaller for O_2

3) Resistivity is greater for O_2, smaller for vacuum.

3.4 Preparation of the Present Samples

The $Co_{1-x}Zn_xFe_2O_4$ (for x = 0.60, 0.80) samples were synthesized using the standard solid state reaction technique which is discussed in section 3.2. Powder of CoO (99.9%), ZnO (99.999%) and Fe_2O_3 (99.99%) were used as raw materials. Stoichiometric amounts of required powders were mixed thoroughly and then calcined at $1100°C$ for 24 hours. The calcined powders were then pressed into toroid shaped samples shown in Fig. 3.3. The samples were sintered at various temperatures ($1100°C$, $1150°C$, $1200°C$, $1250°C$ and $1300°C$) in air for 5 hours and various durations (0.2h, 1h, 5h, 10h and 15h) at $1200°C$ in air. The temperature ramp was $10°C$/minute for both cooling and heating

Figure 3.3 Toroid shaped Samples.

X-ray diffraction study was carried out to determine the sample's structure using an X-ray diffractometer with Cu-K_α radiation. The formation of the single-phase spinel structure was thus confirmed from the diffraction patterns. Results of X-ray diffraction are discussed in Chapter 5.

References

[1]   A. Goldman, *Handbook of Modern Ferromagnetic Materials*, Kulwer Acad. Pub, Boston, U.S.A (1999).

[2]   R. Valenzuela, *Magnetic Ceramics*, Cambridge University Press, Cambridge (1994).

[3]   A. K. M. Akther Hossain, "Investigation of colossal magnetoresistance in bulk and thick film magnetites," *Ph. D. Thesis*, Imperial College, London (1998).

[4]   B. D. Cullity, *Introduction to Magnetic Materials*, Addison-Wisley Publishing Company, Inc., California (1972).

[5]   R. J. Brook, *Sintering: An Overview, Concise Encyclopedia of Advanced Ceramic Materials*, Pergamon Press, Oxford, pp. 438 (1991).

[6]   P. Reijnen, *Science of Ceramics*, Academic Press, London (1967).

[7]   P. I. Slick, *Ferrites for Non-microwave Applications*, Vol. 2. North Holland Pub. Co. (1980).

[8]   W. D. Kingery, H. K. Bowen and D. R. Uhlman, *Introduction to Ceramics*, 2nd edition, Wiley Interscience, Newyork, pp. 476 (1976).

[9]   R. L. Coble and J. E. Burke, *4th Int. Symp. On the Reactivity of Solids*, Amsterdam, pp. 38-51 (1960).

[10]   L. J. McColm and N. J. Clark, *Forming, Shaping and Working of high Performance Ceramics*, Blackie, Glasgow, pp. 1-338 (1988).

CHAPTER 4

EXPERIMENTAL TECHNIQUES

In this chapter we describe basic experimental techniques to measure the lattice parameters and frequency dependent AC permeability of ferrite samples. We describe also the experimental technique for the measurement of temperature dependent initial permeability. The Curie temperatures of the samples were determined from this temperature dependent initial permeability.

4.1 X-ray Diffraction

Bragg reflection is a coherent elastic scattering in which the energy of the X-ray is not changed on reflection. If a beam of monochromatic radiation of wavelength λ is incident on a periodic crystal plane at an angle θ and is diffracted at the same angle as shown in Fig. 4.1, the Bragg diffraction condition for X-rays is given by

$$2d\, Sin\theta = n\lambda \qquad (4.1)$$

where d is the distance between crystal planes and n is the positive integer which represents the order of reflection. Equation (4.1) is known as Bragg law. This Bragg law suggests that the diffraction is only possible when $\lambda \leq 2d$ [1]. For this reason we cannot use the visible light to determine the crystal structure of a material. The X-ray diffraction (XRD) provides substantial information on the crystal structure.
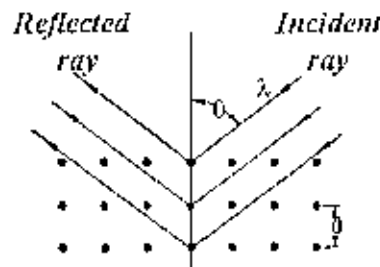

Figure 4.1. Bragg law of diffraction.

X-ray diffraction was carried out with an X-ray diffractometer for the samples $Co_{1-x}Zn_xFe_2O_4$ (where x = 0.60, 0.80). For this purpose monochromatic Cu-K_α radiation

was used. The lattice parameter for each peak of each sample was calculated by using the formula

$$a = d\sqrt{h^2 + k^2 + l^2} \tag{4.2}$$

where *h, k* and *l* are the indices of the crystal planes. To determine the exact lattice parameter for each sample, Nelsion-Riley method was used. The Nelson-Riley function $F(\theta)$ is given as

$$F(\theta) = \frac{1}{2}\left[\left(Cos^2\theta / Sin\theta\right) + \left(Cos^2\theta / \theta\right)\right] \tag{4.3}$$

The values of lattice constant 'a' of all the peaks for a sample are plotted against $F(\theta)$. Then using a least square fit method exact lattice parameter 'a_0' is determined. The point where the least square fit straight line cut the y-axis (i.e. at $F(\theta) = 0$) is the actual lattice parameter of the sample. The theoretical density ρ_{th} was calculated using following expression:

$$\rho_{th} = \frac{8M}{N_A a_0^3} \, g/cm^3 \tag{4.4}$$

where N_A is Avogadro's number (6.02×10^{23} mol^{-1}), M is the molecular weight. The porosity was calculated from the relation $\{100(\rho_{th} - \rho_B)/\rho_{th}\}\%$, where ρ_B is the bulk density measured by the formula $\rho_B = M/V$ [2].

4.2 Microstructural Investigation

The microstructural study of the *Co-Zn* ferrite samples was performed in order to have an insight of the grain structures. The samples of different compositions and sintered at different temperatures were chosen for this purpose. The samples were visualized under a high-resolution optical microscope and then photographed. The pictures were taken at 400 times magnification. Average grain sizes (grain diameter) of the samples were determined from optical micrographs by linear intercept technique [3]. To do this, several random horizontal and vertical lines were drawn on the micrographs. Therefore, we counted the number of grains intersected and measured the length of the grains along the line traversed. Finally the average grain size was calculated.

44

4.3 Complex Permeability Measurement

For high frequency application, the desirable property of a ferrite is high permeability with low loss. One of the most important goals of ferrite research is to fulfill this requirement. The techniques of permeability measurement and frequency characteristics of the present samples are described in sections 4.3.1 and 4.3.2.

4.3.1 Techniques for the Permeability Measurement

Measurements of permeability normally involve the measurements of the change in self-inductance of a coil in presence of the magnetic core. The behaviour of a self-inductance can now be described as follows. We assume an ideal loss less air coil of inductance L_0. On insertion of a magnetic core with permeability μ, the inductance will be μL_0. The complex impedance Z of this coil [4] can be expressed as follows:

$$Z = R + jX = j\omega L_0 \mu = j\omega L_0 (\mu' - j\mu'') \tag{4.5}$$

where the resistive part is $\qquad R = \omega L_0 \mu''$ $\qquad\qquad\qquad$ (4.6)

and the reactive part is $\qquad X = \omega L_0 \mu'$ $\qquad\qquad\qquad\quad$ (4.7)

The RF permeability can be derived from the complex impedance of a coil, Z, given by equation (4.5). The core is taken as toroidal to avoid demagnetizing effects. The quantity L_0 is derived geometrically as shown in section 4.3.2.

4.3.2 Frequency Characteristic Measurement

The frequency characteristics of the Co-Zn ferrite samples i.e. the initial permeability spectra were investigated using an Agilent Impedance Analyzer (model no. 4192A). The complex permeability measurements on toroid shaped specimens were carried out at room temperature on all the samples in the frequency range 1 kHz - 13 MHz. The real part (μ_i') and imaginary part (μ_i'') of the complex permeability were calculated using the following relations [4]: $\mu_i' = L_s/L_0$ and $\mu_i'' = \mu_i' \tan\delta$, where L_s is the self-inductance of the sample core and $L_0 = \mu_0 N^2 S/\pi\overline{d}$ is derived geometrically. Here L_0 is the inductance of the winding coil without the sample core, N is the number

of turns of the coil ($N = 6$), S is the area of cross section of the toroidal sample as given below:

$$S = d \times h,$$

where $$d = \frac{d_2 - d_1}{2},$$

d_1 = Inner diameter,
d_2 = Outer diameter,
h = Height

and $\bar{d}$ is the mean diameter of the toroidal sample as given below

$$\bar{d} = \frac{d_1 + d_2}{2}$$

The relative quality factor is determined from the ratio $\frac{\mu_i'}{\tan \delta}$.

4.4 Curie Temperature Measurement

Curie temperature measurement is one of the most important measurements for magnetic materials. Curie temperature provides substantial information on magnetic status of a substance in respect of the strength of exchange interaction. So, the determination of Curie temperature is of great importance.

Curie temperature was measured from the temperature dependent initial permeability. For this measurement, the sample was kept inside a cylindrical oven with a thermocouple placed at the middle of the sample. The thermocouple measures the temperature inside the oven and also of the sample. The sample was kept just in the middle part of the cylindrical oven in order to minimize the temperature gradient. The temperature of the oven was then raised slowly. If the heating rate is very fast then temperature of the sample may not follow the temperature inside the oven, and there can be misleading information on the temperature of sample. The thermocouple showing the temperature in that case will be erroneous. Therefore, a slow heating rate was used to eliminate this problem. Also, a slow heating ensures accuracy in the determination of Curie temperature. The oven was kept thermally insulated from the surroundings. The temperature dependent permeability was measured at a constant frequency (100 kHz) of a sinusoidal wave.

46

References

[1]   C. Kittel, *Introduction to Solid State Physics*, 7th edition, Jhon Wiley & Sons, Inc., Singapore (1996).

[2]   B. D. Cullity, *Introduction to Magnetic Materials*, Addison-Wisley Publishing Company, Inc., California (1972).

[3]   A. K. M. Akther Hossain, "Investigation of colossal magnetoresistance in bulk and thick film magnetites," *Ph. D Thesis*, Imperial College, London (1998)

[4]   A. Goldman, *Handbook of Modern Ferromagnetic Materials*, Kulwer Acad. Pub, Boston, U.S A (1999)

CHAPTER 5

RESULTS AND DISCUSSION

The polycrystalline $Co_{1-x}Zn_xFe_2O_4$ (x=0.60 and 0.80) ferrites are studied. Various Co-Zn ferrite samples are sintered at various temperatures (1100°C to 1300°C) for five hours and various durations (0.2h to 15h) at 1200°C in air. Structural and surface morphology are studied by x-ray diffraction and optical microscopy. The magnetic properties of the ferrites are characterized with high frequency (1kHz-13MHz) complex permeability, and temperature dependent permeability measurements. The effects of composition, sintering temperature and sintering time on the complex permeability of Co-Zn ferrites are discussed. A possible correlation between sintering temperature, sintering time, density and Curie temperature are also discussed.

5.1 Lattice Parameters, Density and Porosity of the Samples

The X-ray diffraction (XRD) patterns for the samples $Co_{1-x}Zn_xFe_2O_4$ with x = 0.60, 0.80 are shown in Fig. 5.1. Analyzing the XRD patterns, we notice that the positions of the peaks comply with the reported values [1]. The XRD patterns of both compositions clearly indicate their single phase and formation of spinel structure. The positions of the peaks and their corresponding miller indices for the samples investigated are given in Table-5.1. The values of lattice parameter 'a' of all the peaks for both compositions are plotted against Nelson-Riley function, $F(\theta)$, Fig. 5.2. The measured lattice parameter, theoretical density, bulk density, porosity and grain size for different samples sintered at different temperatures and time are given in Tables-5.2 and 5.3 respectively. It is observed that the lattice parameter increases with increasing Zn substitution. The increase in lattice parameter with increasing Zn content can be explained on the basis of the ionic radii. The radius of the Zn^{2+} (0.74 Å) is greater than that of the Co^{2+} (0.72 Å) [1].

Table-5.1. X-ray peak positions for $Co_{1-x}Zn_xFe_2O_4$ samples

Sample composition	X-ray peak position with Miller indices 2θ (degree)					
	(220)	*(311)*	*(400)*	*(422)*	*(511)*	*(440)*
$Co_{0.40}Zn_{0.60}Fe_2O_4$	29.86	35.18	42.88	53.02	56.52	62.1
$Co_{0.20}Zn_{0.80}Fe_2O_4$	29.98	35.26	42.84	53.08	56.58	62.18

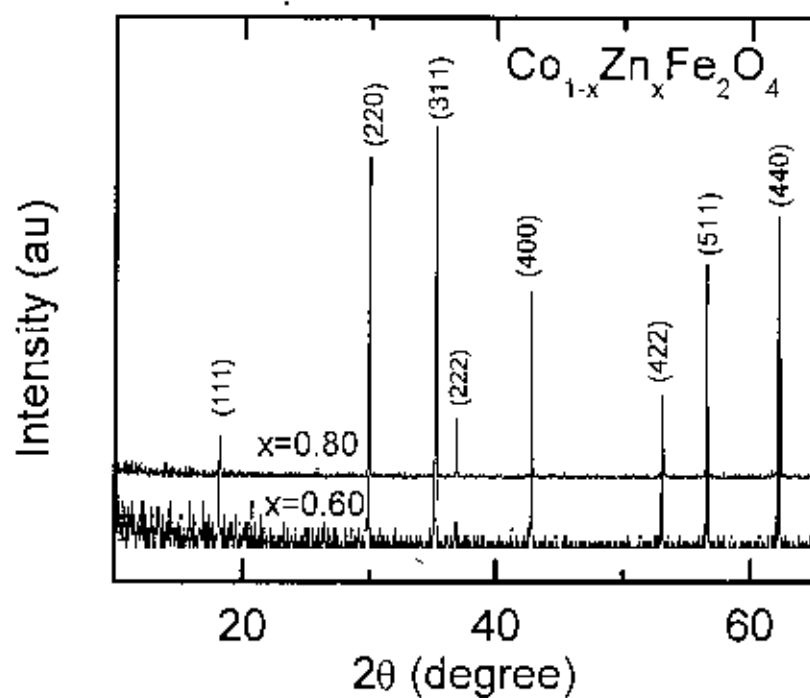**Figure 5.1.** The X-ray diffraction patterns for the samples $Co_{1-x}Zn_xFe_2O_4$ with x = 0.60, 0.80

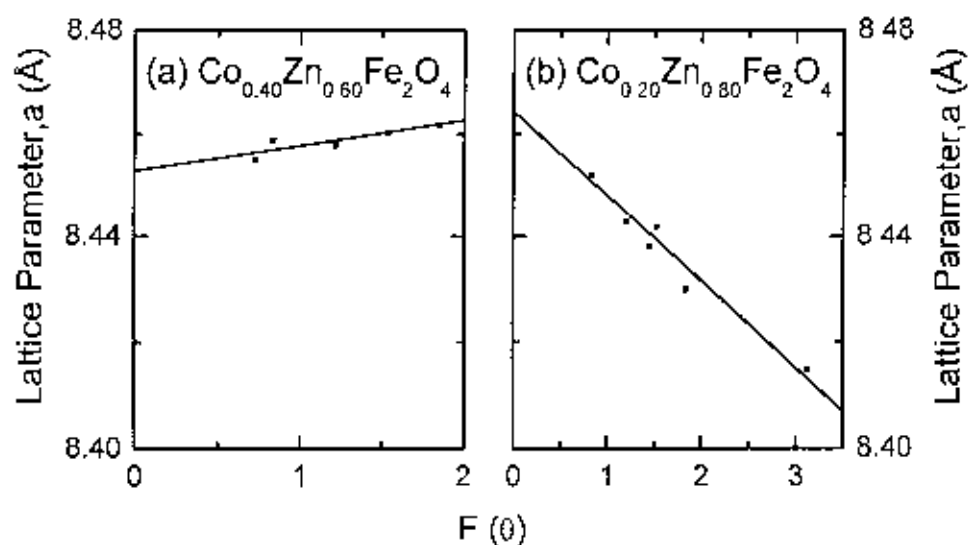**Figure 5.2.** The variation of 'a' with $F(\theta)$ for (a) $Co_{0.40}Zn_{0.60}Fe_2O_4$ and (b) $Co_{0.20}Zn_{0.80}Fe_2O_4$ samples.

Table-5.2. The lattice parameter, density, porosity and average grain size of the $Co_{1-x}Zn_xFe_2O_4$ samples sintered at various temperatures for 5 hours in air

Sample composition	Sintering temperature (°C)	Sintering time (Hours)	a_0 (Å)	ρ_{th} (g/cm³)	ρ_B (g/cm³)	P (%)	<Grain size> (μm)
$Co_{0.40}Zn_{0.60}Fe_2O_4$	1100	5	8.4528	5.2456	4.115	21.55	
	1150				4.623	11.87	
	1200				4.753	9.38	
	1250				4.825	8.01	
	1300				4.746	9.52	9.557
$Co_{0.20}Zn_{0.80}Fe_2O_4$	1100	5	8.4644	5.2524	4.350	17.17	
	1150				4.670	11.08	
	1200				4.736	9.83	
	1250				4.730	9.94	
	1300				4.698	10.54	10.402

Table-5.3. The lattice parameter, density and porosity of the $Co_{1-x}Zn_xFe_2O_4$ samples sintered at various durations at 1200°C in air.

Sample composition	Sintering temperature (°C)	Sintering time (Hours)	a_0 (Å)	ρ_{th} (g/cm³)	ρ_B (g/cm³)	P (%)
$Co_{0.40}Zn_{0.60}Fe_2O_4$	1200	0.2	8.4528	5.2456	4.535	13.54
		1			4.536	13.52
		5			4.685	10.68
		10			4.734	9.75
		15			4.784	8.79
$Co_{0.20}Zn_{0.80}Fe_2O_4$	1200	0.2	8.4644	5.2524	4.611	12.21
		1			4.728	9.98
		5			4.710	10.32
		10			4.661	11.27
		15			4.610	12.23

Figure 5.3 shows the density and porosity as a function of sintering temperature, T_s, for both compositions. The density of the $Co_{0.40}Zn_{0.60}Fe_2O_4$ samples increases as the sintering temperature increases from 1100°C to 1250°C and above 1250°C the density decreases slightly. On the other hand, porosity (P) of the sample decreases as increasing sintering temperature up to 1250°C, and above 1250°C the porosity increases slightly.

The $Co_{0.20}Zn_{0.80}Fe_2O_4$ samples show similar behaviour of changes to that of $Co_{0.40}Zn_{0.60}Fe_2O_4$ samples except that density is found to be maximum at $1200°C$. It is known that the porosity of ceramic samples results from two sources, intragranular porosity and intergranular porosity [2]. Thus the total porosity could be written as $P=P_{intra}+P_{inter}$ The intergranular porosity mainly depends on the grain size [2]. At higher sintering temperatures the density decreases because the intragranular porosity increases resulting from discontinuous grain growth. Such a conclusion is in agreement with that previously reported in case of $MgCuZn$ ferrites [3].
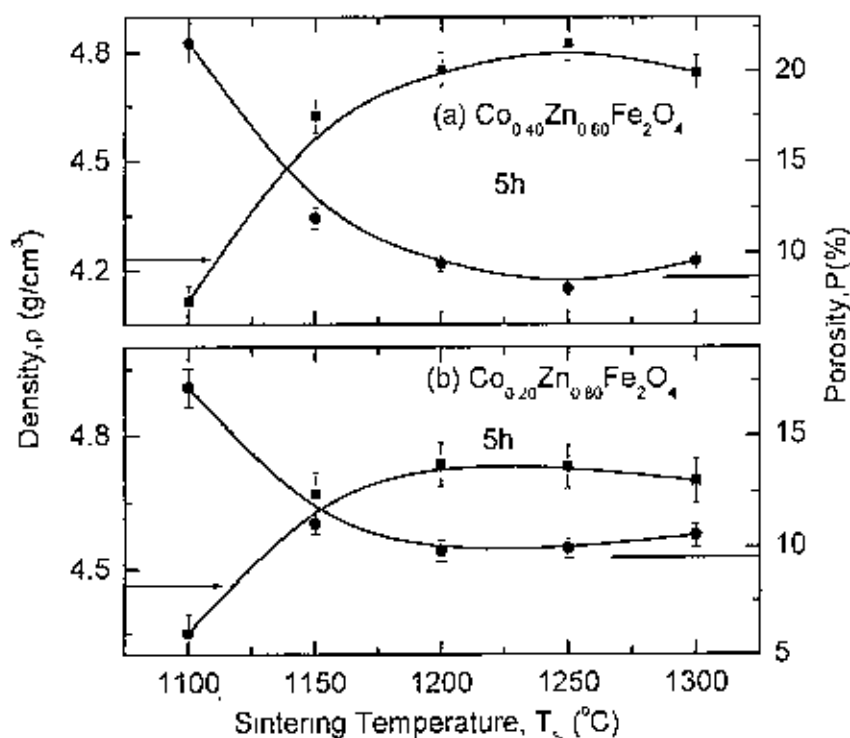

Figure 5.3. The variation of density (■) and porosity (●) with sintering temperature for (a) $Co_{0.40}Zn_{0.60}Fe_2O_4$ and (b) $Co_{0.20}Zn_{0.80}Fe_2O_4$ samples.

Figure 5.4 shows the density and porosity as a function of sintering time for the both compositions sintered at $1200°C$ temperatures. The density of the $Co_{0.40}Zn_{0.60}Fe_2O_4$ samples increases slowly as the sintering time increases from 0.2h to 1h and above 1h the density increases rapidly. On the other hand, porosity (P) of the sample decreases as

increasing sintering time. The $Co_{0.20}Zn_{0.80}Fe_2O_4$ samples show different behaviour of changes to that of $Co_{0.40}Zn_{0.60}Fe_2O_4$. The density of the $Co_{0.20}Zn_{0.80}Fe_2O_4$ samples increases rapidly as the sintering time increases from 0.2h to 1h and above 1h the density decreases slowly. The maximum density is obtained for the $Co_{0.40}Zn_{0.60}Fe_2O_4$ samples sintered for 15h while for $Co_{0.20}Zn_{0.80}Fe_2O_4$ samples it is obtained for 1h sintering time.
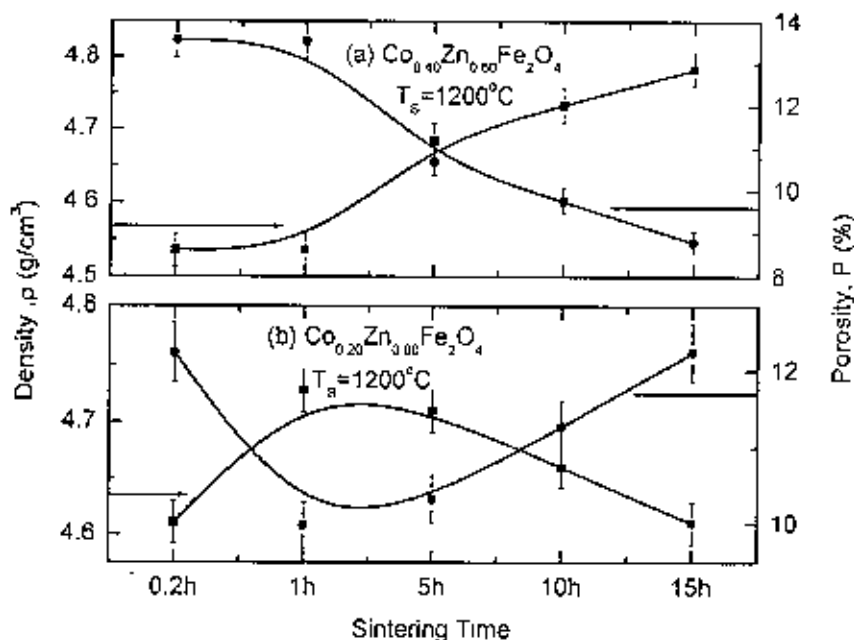

Figure 5.4. The variation of density (■) and porosity (●) with sintering time for (a) $Co_{0.40}Zn_{0.60}Fe_2O_4$ and (b) $Co_{0.20}Zn_{0.80}Fe_2O_4$ samples.

5.2 Microstructures of $Co_{1-x}Zn_xFe_2O_4$

The optical micrographs of $Co_{0.40}Zn_{0.60}Fe_2O_4$ and $Co_{0.20}Zn_{0.80}Fe_2O_4$ samples sintered at 1300°C in air for 5 hours are shown in Figs. 5.5 and 5.6, respectively. The black areas are voids. The average grain sizes for the both compositions are determined by linear intercept technique and are presented in Table 5.2.

It is observed that the sample composition has an influence on the enhancement of grain size. The average grain sizes for the sample $Co_{0.20}Zn_{0.80}Fe_2O_4$ are greater than

that of $Co_{0.40}Zn_{0.60}Fe_2O_4$. Therefore the average grain size of the sample increases with increasing zinc substitution.

25 μm

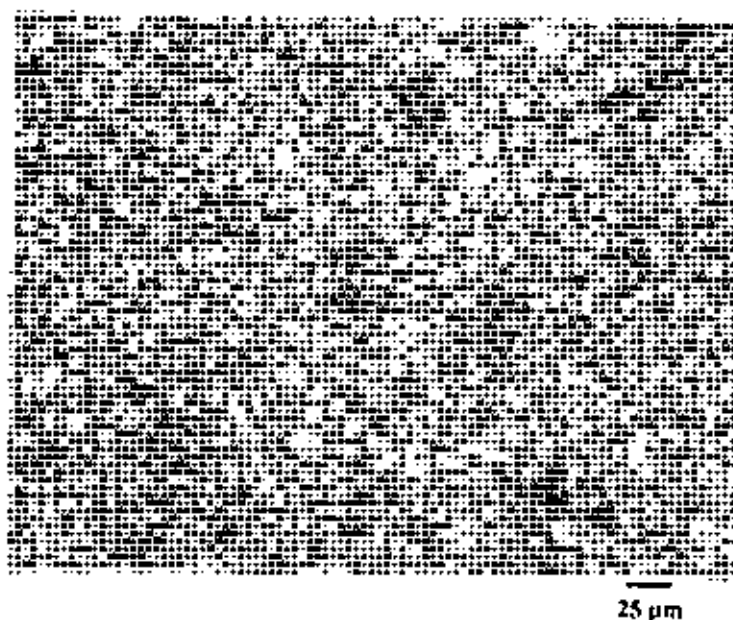Figure 5.5. The optical micrograph of $Co_{0.42}Zn_{0.60}Fe_2O_4$ sample sintered at temperature 1300°C in air for 5 hours.

25 μm
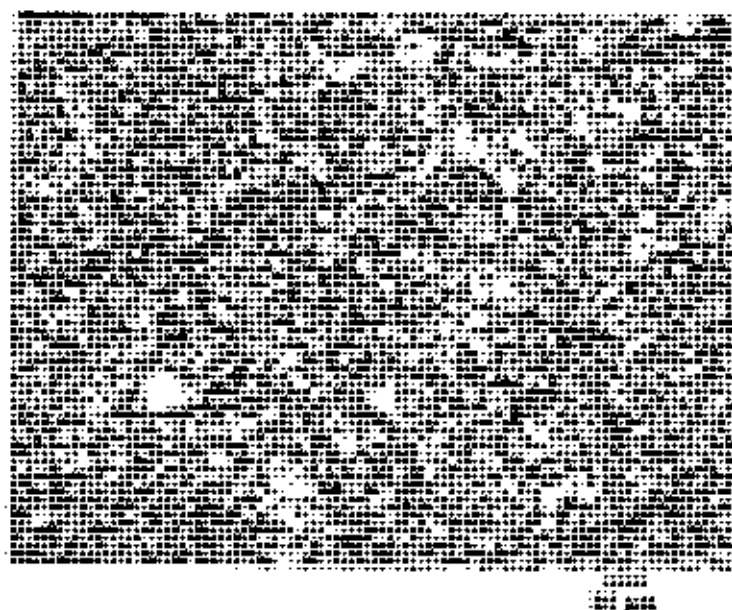
Figure 5.6. The optical micrograph of $Co_{0.40}Zn_{0.60}Fe_2O_4$ sample sintered at temperature 1300°C in air for 5 hours.

The grain size reflects the presence of more or less grain boundary area. Even porosity may be strongly related to boundaries since they can remove porosity. The uniformity in the grain size and the average grain diameter can control properties of materials such as the magnetic permeability. When the grain growth rate is very high, pores may be left behind by rapidly moving grain boundaries, resulting in pores that are trapped inside the grains. This intragranular porosity is practically impossible to eliminate, leading to poor magnetic and mechanical properties.

The behaviour of grain growth reflects the competition between the driving force for grain boundary movement and the retarding force exerted by pores [4]. During the sintering process, the thermal energy generates a force that drives the grain boundaries to grow over pores, thereby decreasing the pore volume and densifying the material. When the driving force of the grain boundary in each grain is homogeneous, the sintered body attains a uniform grain size distribution; in contrast, discontinuous grain growth occurs if this driving force is inhomogeneous. The discontinuous growth of grain rises with temperature, hindering the migration of the pore to the grain boundary and hence, contributing toward the reduction of the sintered density.

5.3 Complex Permeability

Figures 5.7 and 5.8 show the real and imaginary permeability spectra for $Co_{0.40}Zn_{0.60}Fe_2O_4$ and $Co_{0.20}Zn_{0.80}Fe_2O_4$ samples sintered at various temperatures (1100°C to 1300°C) for five hours, respectively. The permeability value increases with increasing Co content in $Co_{1-x}Zn_xFe_2O_4$. With the increase of sintering temperature, T_s the real part of the initial permeability is found to increase at first and then decreases. In case of $Co_{0.40}Zn_{0.60}Fe_2O_4$ samples, μ_i' increases as the T_s increases up to 1250°C and above 1250°C, μ_i' decreases. The $Co_{0.20}Zn_{0.80}Fe_2O_4$ samples show similar change of permeability to that of $Co_{0.40}Zn_{0.60}Fe_2O_4$ samples except that μ_i' is found to be maximum at 1200°C.

Figure 5.7. (a) The real and (b) imaginary permeability spectra for $Co_{0.40}Zn_{0.60}Fe_2O_4$ samples sintered at temperatures 1100°C, 1150°C, 1200°C, 1250°C and 1300°C in air for 5 hours.

Figure 5.8. (a) The real and (b) imaginary permeability spectra for $Co_{0.20}Zn_{0.80}Fe_2O_4$ samples sintered at temperatures 1100°C, 1150°C, 1200°C, 1250°C and 1300°C in air for 5 hours.

Figures 5.9 and 5.10 show the real and imaginary permeability spectra for $Co_{0.40}Zn_{0.60}Fe_2O_4$ and $Co_{0.20}Zn_{0.80}Fe_2O_4$ samples sintered at various durations (0.2h to 15h) at 1200°C in air. The initial permeability of the $Co_{0.40}Zn_{0.60}Fe_2O_4$ samples increases slowly as the sintering time increases from 0.2h to 1h and above 1h initial permeability increases rapidly (Fig. 5.12). The maximum initial permeability is obtained for the sample sintered for 15h.

On the other hand the initial permeability of the $Co_{0.20}Zn_{0.80}Fe_2O_4$ samples increases rapidly as the sintering time increases from 0.2h to 1h and above 1h initial permeability decreases slowly (Fig. 5.12). The maximum initial permeability is obtained for the sample sintered for 1h.

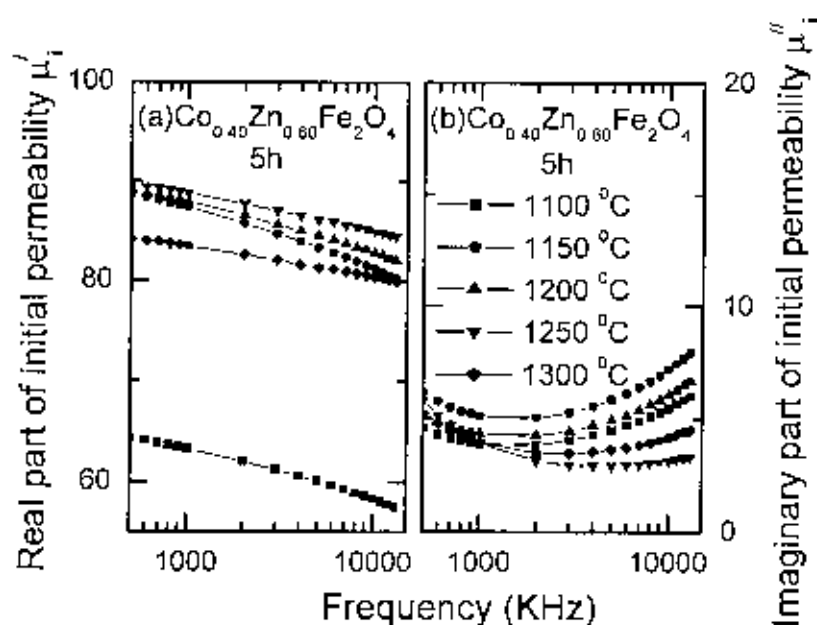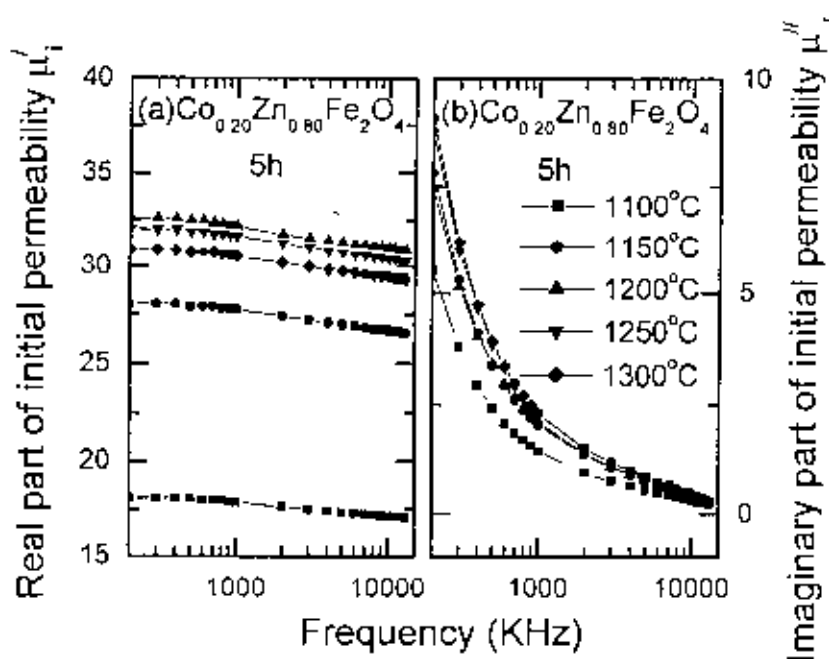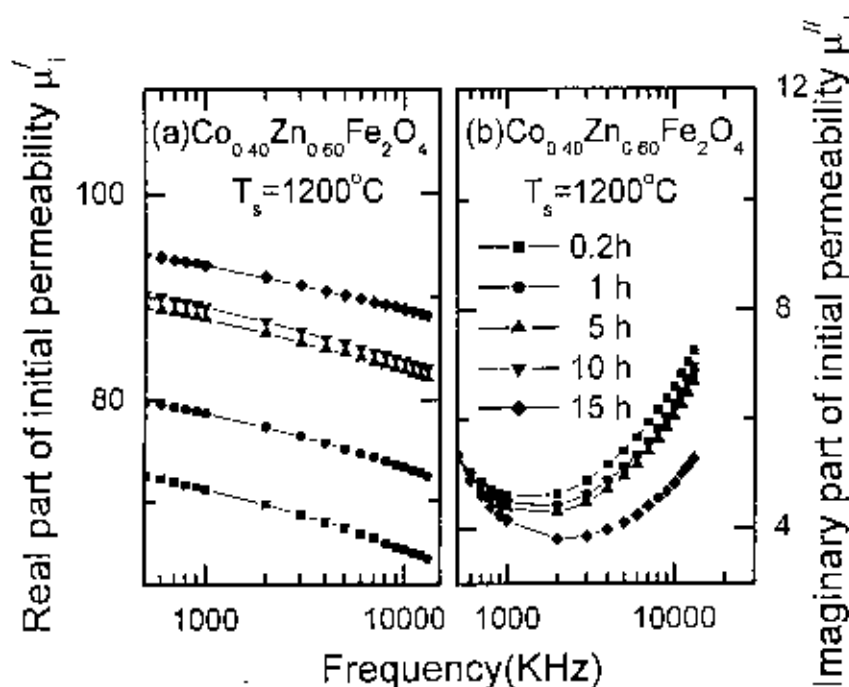**Figure 5.9.** (a) The real and (b) imaginary permeability spectra for $Co_{0.40}Zn_{0.60}Fe_2O_4$ samples sintered at temperature 1200°C for 0.2h, 1h, 5h, 10h and 15h in air.

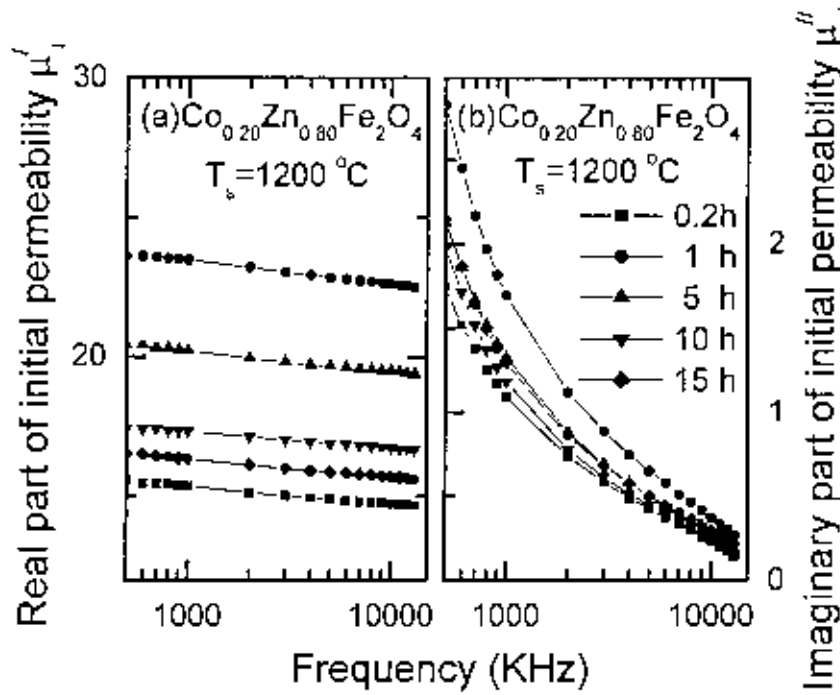**Figure 5.10.** (a) The real and (b) imaginary permeability spectra for $Co_{0.20}Zn_{0.80}Fe_2O_4$ samples sintered at temperature $1200°C$ for 0.2h, 1h, 5h, 10h and 15h in air.

It is well known that the permeability of polycrystalline ferrite is related to two different magnetizing mechanisms: spin rotation and domain wall motion [5, 6], which can be described as follows:

$$\mu_i = 1 + \chi_w + \chi_{spin}$$

where χ_w is the domain wall susceptibility; χ_{spin} is intrinsic spin rotational susceptibility. χ_w and χ_{spin} may be written as : $\chi_w = 3\pi M_s^2 D/4\gamma$ and $\chi_{spin} = 2\pi M_s^2/K$ with M_s saturation magnetization, K the anisotropy constant, D the average grain diameter, and γ the domain wall energy. Thus the domain wall motion is affected by the grain size and enhanced with the increase of grain size. The initial permeability is therefore a function of grain size. The magnetization caused by domain wall movement requires less energy than that required by domain rotation.

One can expect higher μ_i' for the sample sintered at higher T_s. However, we have observed that for both the compositions μ_i' is found to be maximum at optimum T_s

57

(depending on sample composition) as shown in Fig. 5.11. If the sintering temperature is higher than that of the optimum T_s, μ_i' decreases. It is possible that the samples sintered at higher sintering temperatures (> optimum T_s) may increase the number of pores within the grains which results in a decrease of permeability and also density. Similar behavior was observed by Mahmud et al. [7] in *Ni-Zn* and Guillaud [8] in *Mn-Zn* ferrites. It is possible that if pores are located at the grain boundaries, the permeability may increase with grain size. The relationship between grain size and permeability would generally be linear only if the grain growth is normal, that is, if all the grains grow pretty much at the same time and same rate. Porosity at the grain boundaries is less damaging to the permeability, because it causes less hindrance to domain wall motion than porosity within grains. If, indeed, some grains grew very rapidly, they would trap pores, which as we have seen, can limit permeability by pinning domain walls. For the composition of $Co_{0.40}Zn_{0.60}Fe_2O_4$ sintered at temperature $1200°C$ for 15h, the increase of μ_i' is pronounced (Fig. 5.12). This is because the sintered density is highest for this temperature and time.
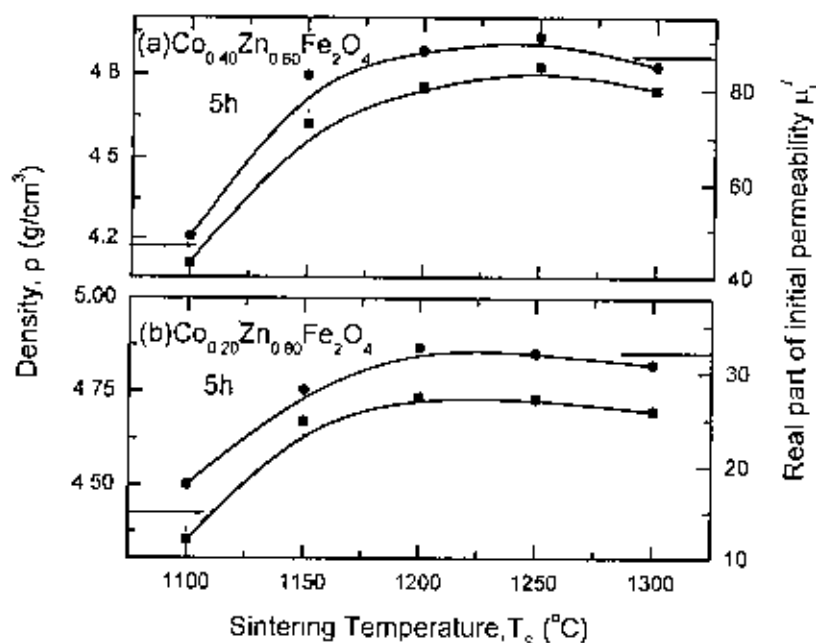
Figure 5.11. The variation of μ_i' and ρ with T_s for (a) $Co_{0.40}Zn_{0.60}Fe_2O_4$ and (b) $Co_{0.20}Zn_{0.80}Fe_2O_4$ samples sintered for 5h.

58
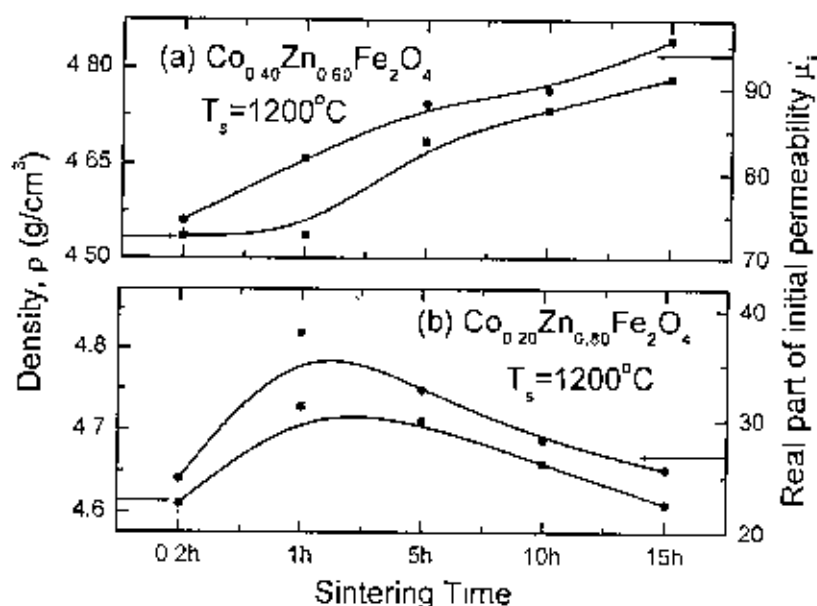
Figure 5.12. The variation of μ_i' and ρ with sintering time for (a) $Co_{0.40}Zn_{0.60}Fe_2O_4$ and (b) $Co_{0.20}Zn_{0.80}Fe_2O_4$ samples sintered at 1200°C

If the applied alternating magnetic field is weak, at high frequencies, the domain wall will oscillate back and forth through a small distance about the mean position. The differential equation for oscillating boundaries can be written as $md^2x/dt^2 + \beta dx/dt + \alpha x = 2M_s H(t)$. where m is the effective wall mass, β the damping factor, α the restoring constant, x the wall displacement and $H(t)$ the driving force [9,10,11]. The first term on the left hand side represents the wall inertia; the second term is the damping opposing the propagation velocity, and the third term is associated with wall pinning to defects, expressed as a restoring force.

Energy loss is an extremely important subject in soft ferrimagnetic materials, since the amount of energy wasted on process other than magnetization can prevent the AC applications of a given material. The ratio of μ_i' and μ_i'' representing the losses in the material are a measure of the inefficiency of the magnetic system. Obviously this parameter should be as low as possible. The magnetic losses, which cause the phase shift, can be split up into three components: hysteresis losses, eddy current losses and

residual losses. This gives the formula $\tan \delta_m = \tan \delta_h + \tan \delta_e + \tan \delta_r$. μ_i is the initial permeability which created at low field. Hysteresis losses vanish at very low field strengths. Thus at low field the remaining magnetic losses are eddy current losses and residual losses. Residual losses are independent of frequency. Eddy current losses increase with frequency and are negligible at very low frequency. Eddy current loss can be expressed as $P_e \approx f^2 / \rho$, where P_e is the energy loss per unit volume and ρ is the resistivity [9]. To keep the eddy current losses constant as frequency is increased: the resistivity of the material chosen must increase as the square of frequency. Eddy currents are not problem in the *Co-Zn* ferrites until higher frequencies are encountered because they have very high resistivity about $10^5 \Omega cm$ to $10^8 \Omega cm$ [12]. The ferrite microstructure is assumed to consist of grains of low resistivity separated by grain boundaries of high resistivity. Thicker grain boundaries are preferred to increase the resistance. Figure. 5.13 shows the variations of loss factors with frequency of the two compositions of the samples sintered at different sintering temperature T_s for 5 hours. On the other hand Fig. 5.14 shows the variations of loss factors with frequency of the two compositions of the samples sintered for different sintering time at constant sintering temperature $1200^\circ C$. For the samples $Co_{0.40}Zn_{0.60}Fe_2O_4$ the magnetic loss is minimum between frequencies 1MHz and 4MHz while for $Co_{0.20}Zn_{0.80}Fe_2O_4$ samples this loss is minimum above 13MHz (Figs. 5.13 and 5.14).
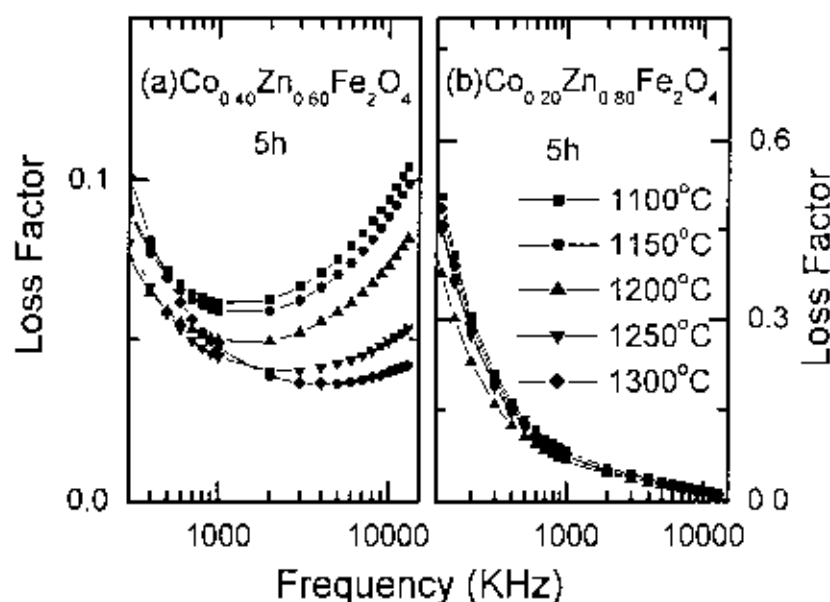
Figure 5.13. The variation of Loss factors with frequency for (a) $Co_{0.40}Zn_{0.60}Fe_2O_4$ and (b) $Co_{0.20}Zn_{0.80}Fe_2O_4$ samples sintered at different sintering temperatures T_s for 5 hours.
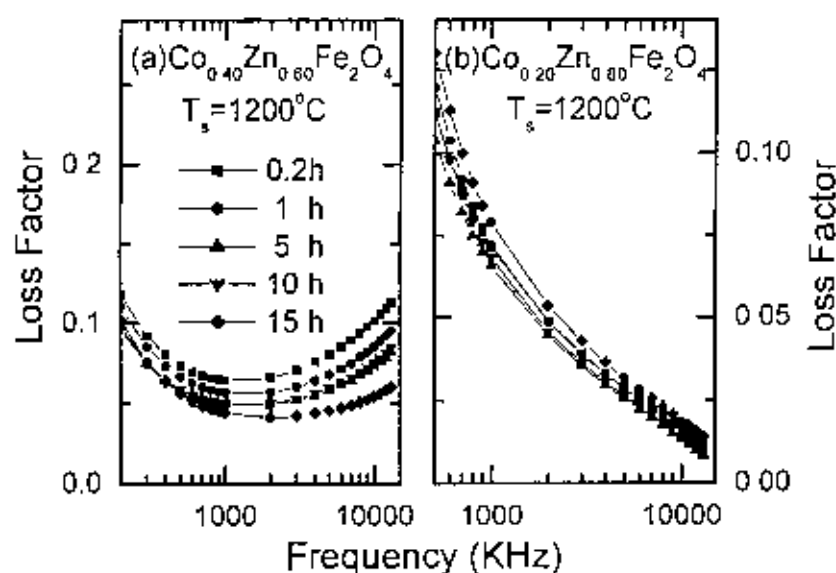
Figure 5.14. The variation of Loss factors with frequency for (a) $Co_{0.40}Zn_{0.60}Fe_2O_4$ and (b) $Co_{0.20}Zn_{0.80}Fe_2O_4$ samples sintered for different sintering time at constant sintering temperature 1200°C.

From the loss factor we have calculated the relative quality factor (or Q factor) for both compositions sintered at various temperatures and various durations. The Q factors are shown in Figs. 5.15 and 5.16. For inductors used in filter applications, the quality factor is often used as a measure of performance. It is observed that the sample sintered at 1300°C has highest Q value for $Co_{0.40}Zn_{0.60}Fe_2O_4$. The highest Q value for $Co_{0.40}Zn_{0.60}Fe_2O_4$ is found to be 2.25×10^3 at frequency 4MHz at 1300°C sintering temperature. The highest Q value for $Co_{0.20}Zn_{0.80}Fe_2O_4$ samples is not found between our frequency range (1KHz to 13MHz) because it exist above 13MHz frequency.
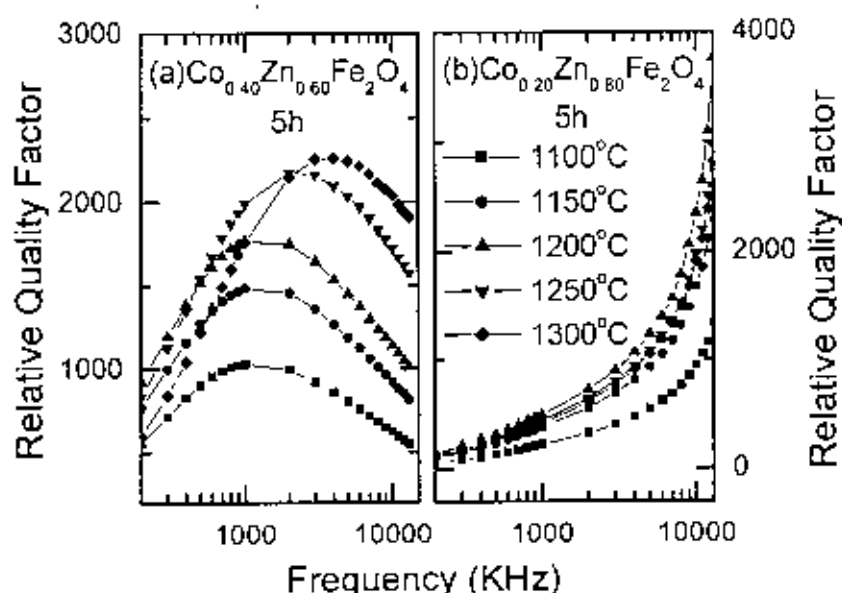
Figure 5.15. The variation of Q factors with frequency for (a) $Co_{0.40}Zn_{0.60}Fe_2O_4$ and (b) $Co_{0.20}Zn_{0.80}Fe_2O_4$ samples sintered at different sintering temperatures T_s for 5 hours.

62
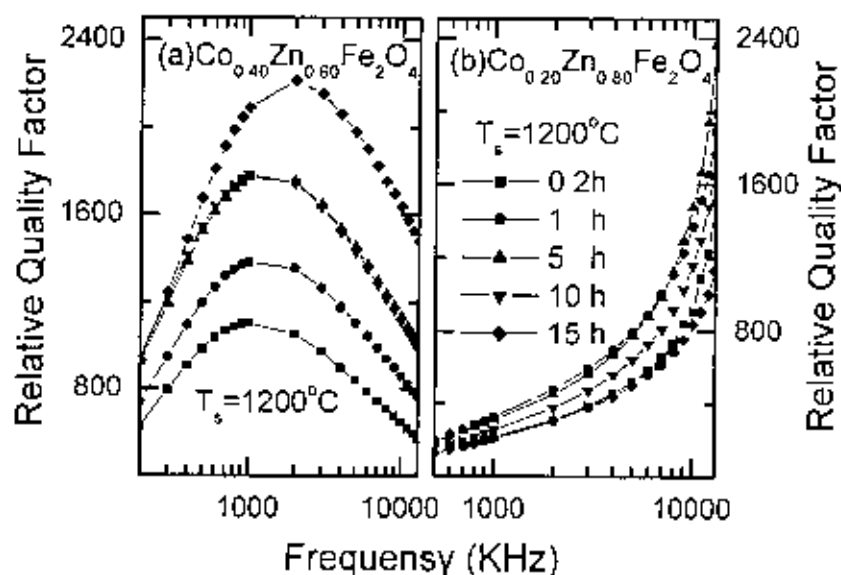
Figure 5.16. The variation of Q factors with frequency for (a) $Co_{0.40}Zn_{0.60}Fe_2O_4$ and (b) $Co_{0.20}Zn_{0.80}Fe_2O_4$ samples sintered for different sintering time at constant sintering temperature 1200°C.

5.4 Magnetic Properties

5.4.1 DC Magnetization

The variation of magnetization as a function of temperature, $M(T)$, for various $Co_{1-x}Zn_xFe_2O_4$ samples is shown in Fig. 5.17. The samples are sintered at 1200°C for 5 h. The data is taken in the presence of 1T applied magnetic field in Field cooled (FC) condition. It is observed that the $Co_{0.20}Zn_{0.80}Fe_2O_4$ sample undergo paramagnetic to ferrimagnetic transition at a temperature, T_c, 170K. The T_c of $Co_{0.40}Zn_{0.60}Fe_2O_4$ sample is above 350 K and can not be determined from the present $M(T)$ curve. The T_c of this sample is determined from the AC magnetization measurement (to be discussed in the section 5.4.2). It is observed that the sample which contains higher concentration of Zn has lower T_c. This is due to the fact that inclusion of nonmagnetic Zn weakens the A-B magnetic interaction among the cations and hence decreases the T_c. Also the sample which has higher Zn concentration has lower magnetization.
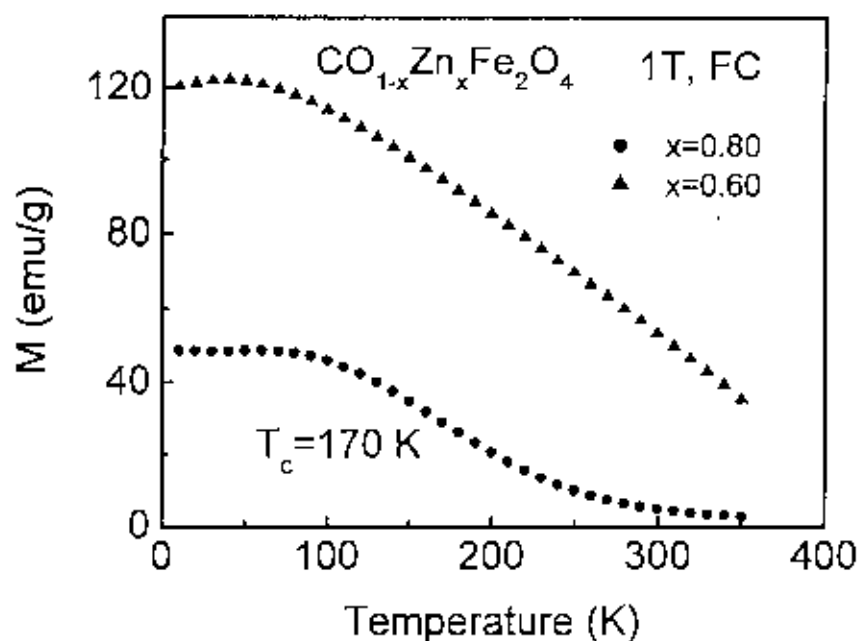
Figure 5.17. The temperature dependence of magnetization for $Co_{1-x}Zn_xFe_2O_4$ (x=0.60, 0.80) samples measured in presence of 1T applied field in Field cooled (*FC*) mode. Samples sintered at $1200^{\circ}C$ for 5 h in air.

The magnetisation as a function of applied magnetic field, *M-H*, for various $Co_{1-x}Zn_xFe_2O_4$ samples at room temperature (300K) is shown in Fig. 5.18. The magnetization of $Co_{0.40}Zn_{0.60}Fe_2O_4$ sample increases linearly with increasing the applied magnetic field up to 0.1T applied magnetic field. Beyond 0.1T applied field magnetisation increases slowly. No saturation is observed in the presence of 1T applied magnetic filed, suggest that this sample is not a collinear ferrimagnet rather *B* site cations are canted. The $Co_{1-x}Zn_xFe_2O_4$ ferrite is a mixed spinel type with a general formula $Zn_xFe_{1-x}[Co_{1-x}Fe_{1+x}]O_4$, where the term within the square brackets indicates the octahedral (*B*) sites and the first term is tetrahedral (*A*) sites. As the magnetic filed increases canting angle of *B* site cations decreases and hence increases the magnetisation. This type of spinel ferrites are known as Yafet-Kittel type ferrites [1.13].
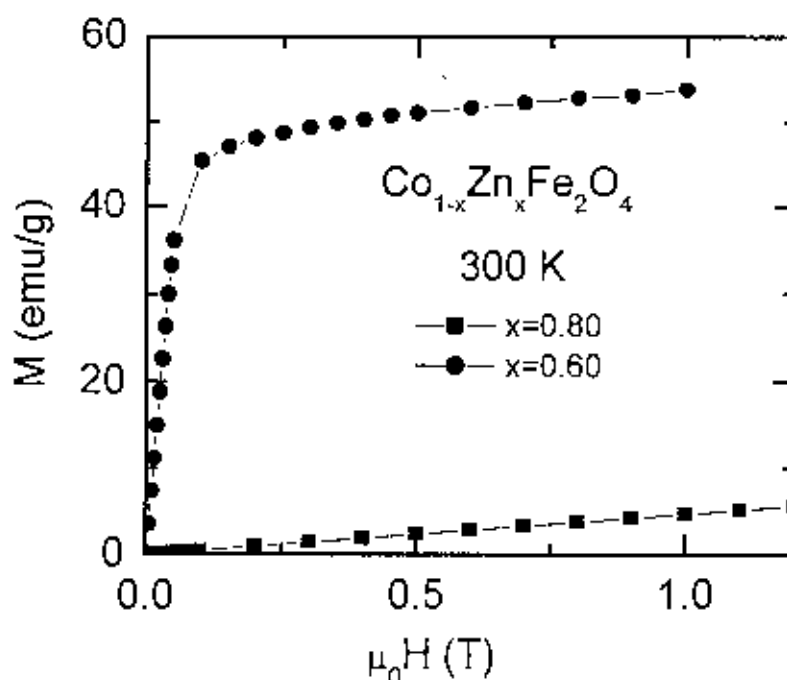
Figure 5.18. The *M-H* curves of $Co_{1-x}Zn_xFe_2O_4$ (x=0.60, 0.80) samples measured at 300 K. Samples were sintered at 1200°C for 5 h in air.

On the other hand, the magnetization increases linearly with *H* for the sample $Co_{0.20}Zn_{0.80}Fe_2O_4$ suggesting that this sample is paramagnetic at this temperature. Therefore, from this figure it is clear that at room temperature the sample $Zn_{0.60}Co_{0.40}Fe_2O_4$ is in ferrimagnetic state while the sample $Co_{0.20}Zn_{0.80}Fe_2O_4$ is in paramagnetic state.

5.4.2 Temperature Dependent Initial Permeability and Curie Temperature

Real part of the initial permeability, μ_i', as a function of temperature for $Co_{0.40}Zn_{0.60}Fe_2O_4$ samples sintered at various temperatures for 5 hours are shown in Fig. 5.19. From these curves the T_c's of these samples are determined. It is observed that the T_c slightly increases with increasing sintering temperature for the $Co_{0.40}Zn_{0.60}Fe_2O_4$ composition. The values of T_c's are 330K, 351K, 374K and 397K for samples sintered at 1100°C, 1200°C, 1250°C and 1300°C for 5 hours respectively. The T_c values were

determined from the minima of the derivative of $\mu_i'(T)$ curves. It was found that the sample sintered at 1250°C has a sharp transition from ferrimagnetic to paramagnetic state compared with the samples sintered at 1100°C, 1200°C and 1300°C for 5 hours. From this result it can be assumed that the optimum sintering temperature is 1250°C for the $Co_{0.40}Zn_{0.60}Fe_2O_4$ composition.
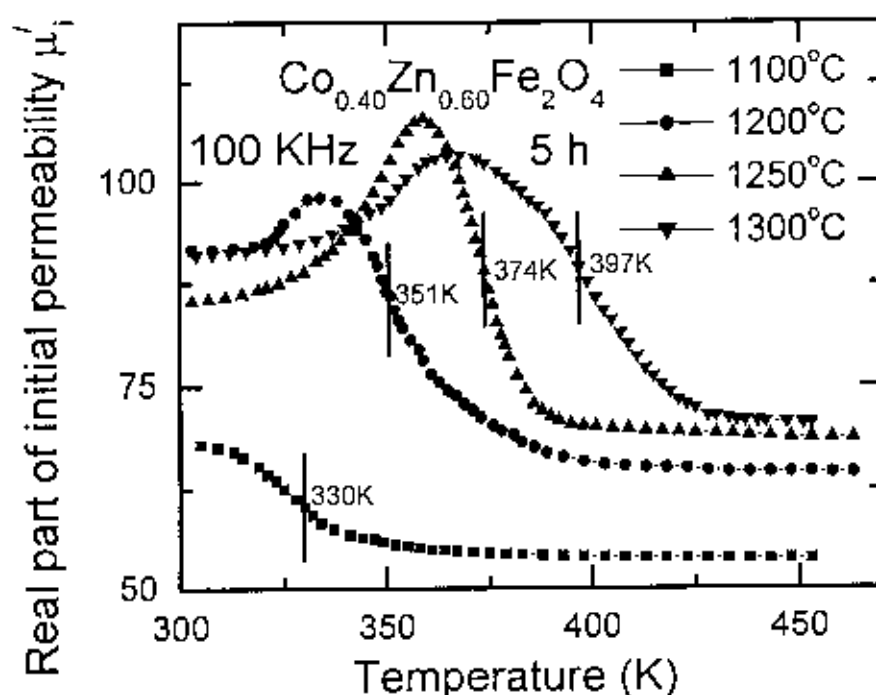
Figure 5.19. Initial permeability as a function of temperature for $Co_{0.40}Zn_{0.60}Fe_2O_4$ samples sintered at various temperatures for 5hours.

Real part of the initial permeability, μ_i', as a function of temperature for $Co_{0.40}Zn_{0.60}Fe_2O_4$ samples sintered at 1200°C for various durations are shown in Fig. 5.20. From these curves the T_c's of these samples are determined. It is observed that the T_c slightly increases with increasing sintering time for the $Co_{0.40}Zn_{0.60}Fe_2O_4$ composition. The values of T_c's are 343K, 351K and 359K for samples sintered at 1200°C for 1h, 5h and 15 h, respectively. It was found that the sample sintered at

66

1200°C for 1h and 15h have a transition with an additional shoulder at high temperature region. On the other hand for the sample sintered for 5h has a relatively smooth transition. This is probably due to the effect of grain boundary, inhomogeneity and other defects in the samples. From this result it can be assumed that the optimum sintering time is 5h for this composition. The present values of T_c's are in close agreement with the published results [14]. The variations among the present results and the published results could be related to the variation of the preparation condition.

For applications, the temperature dependence of μ_i' is very important. The initial permeability of the substances as a function of temperature is measured at a constant frequency (100 kHz) of a sinusoidal wave. It is observed that the permeability falls sharply when the magnetic state of the ferrite samples changes from ferrimagnetic to paramagnetic. The vertical drop of the permeability at the Curie point indicates the degree of homogeneity in the sample composition [15, 16]. The degree of homogeneity of our samples has shown is not so good. Measurement of the initial permeability as a function of temperature can therefore be used as a material characterization method. The T_c for different samples is given in Table-5.4.
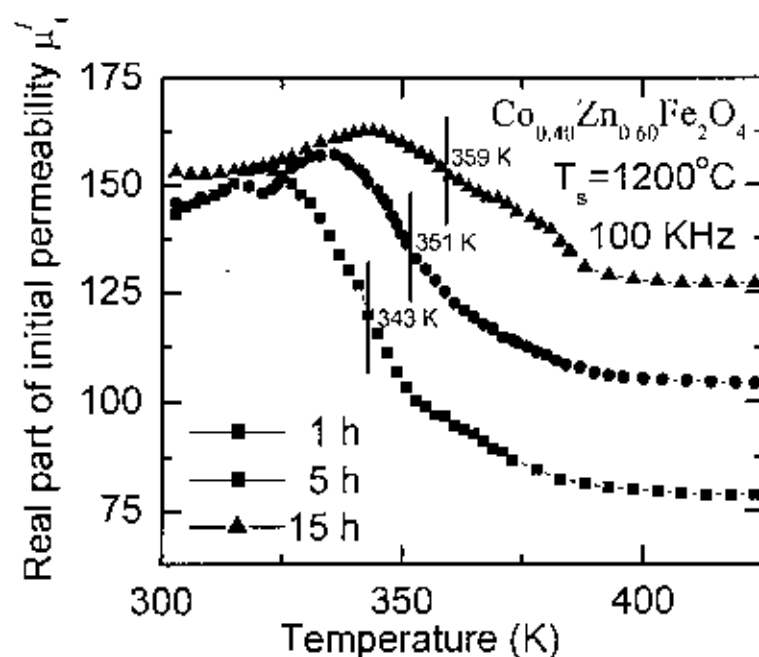
Figure 5.20. Initial permeability as a function of temperature for $Co_{0.40}Zn_{0.60}Fe_2O_4$ samples sintered at 1200°C for various durations.

It is noted that the samples of two compositions contain different Zn contents. It is observed from the Fig. 5.17 that the T_c is lower when Zn content is higher. This is expected because of the inclusion of higher concentration of non-magnetic Zn in the materials. This is in harmony with the theoretical and experimental findings. It is also observed that the T_c is slightly increased with increasing sintering temperature.

Table-5.4. The Curie temperature, T_c of $Co_{0.40}Zn_{0.60}Fe_2O_4$ samples.

Sample composition	Sintering time (hours)	Sintering temperature (°C)	Curie temperature (K)
$Co_{0.40}Zn_{0.60}Fe_2O_4$	5	1100	330
		1200	351
		1250	374
		1300	397
$Co_{0.40}Zn_{0.60}Fe_2O_4$	1	1200	343
	5		351
	15		359

Co-Zn ferrite is a mixed normal-inverse spinel type with a general formula $Zn_xFe_{1-x}[Co_{1-x}Fe_{1+x}]O_4$, where the term within the square brackets indicates the octahedral (B) sites and the first term is tetrahedral (A) sites. The decrease of T_c with an increasing Zn content may be explained by a modification of the A-B exchange interaction strength due to the change of the Fe^{3+} distribution between A and B sites. The decrease of the Curie temperature is due to the weakening of the A-B interaction. This could be attributed to the increase in distance between the moments of A and B sites, which is confirmed by the increase in the lattice parameter with increasing Zn content. The larger distances between moments in samples $Co_{0.20}Zn_{0.80}Fe_2O_4$ leads to decrease the A-B interaction relative to that of $Co_{0.40}Zn_{0.60}Fe_2O_4$ samples and consequently the T_c decreases.

Anisotropy constants vary considerably with temperature. In most cases, anisotropy decreases steeply from a high value at low temperature and then slowly decreases down to zero at T_c [9]. There is then no preferred crystallographic direction for the magnetization of a domain. It is observed that the initial permeability, μ_i', increases with temperature to a maximum value just below the T_c. This occurs, because the crystal anisotropy normally decreases with increasing temperature [17]. The initial permeability varies as $\mu_i \approx M_s^2 / K_1^{1/2}$ [9,18]. Since anisotropy decreases faster than magnetization on heating, the initial permeability expectantly increases with temperature, tends to infinity just below the T_c and then drops for the paramagnetic phase. The peak near T_c is known as the 'Hopkinson' peak [9].

References

[1]   A. K. M. Akther Hossain, M. Seki, T. Kawai and H. Tabata, "Colossal magnetoresistance in spinel type $Zn_{1-x}Ni_xFe_2O_4$," *J. Appl. Phys.*, **96**, 1273 (2004).

[2]   A. A. Sattar, H. M. El-Sayed, K. M. El-Shokrofy and M. M. El-Tabey, "Improvement of the magnetic properties of Mn-Ni-Zn ferrite by the non-magnetic Al^{3+} ion substitution," *J. Appl Sci.*, **5**(1), 162 (2005).

[3]   S. R. Murthy, "Low temperature sintering of MgCuZn ferrite and its electrical and magnetic properties," *Bull. Mater. Sci.*, **24**(4), 379 (2001).

[4]   A. C. F. M. Costa, E. Tortella, M. R. Morelli and R. H. G. A. Kiminami, " Synthesis, microstructure and magnetic properties of Ni-Zn ferrites," *Journal of Magnetism and Magnetic Materials*, **256**, 174 (2003).

[5]   Hu Jun and Yan Mi, "Preparation of high permeability Ni-Cu-Zn ferrite," *Journal of Zhejiang University Science*, **6B**(6), 580 (2005).

[6]   T. Tsutaoka, M. Ueshima, T. Tokunaga, T. Nakamura and K. Hatakeyama, "Frequency dispersion and temperature variation of complex permeability of Ni-Zn ferrite composite materials," *J. Appl. Phys.*, **78**(6), 3983 (1995).

[7]   S. T. Mahmud, A. K. M. Akther Hossain, A. K. M. Abdul Hakim, M. Seki, T. Kawai and H. Tabata, "Influence of microstructure on the complex permeability of spinel type Ni-Zn ferrite," *Journal of Magnetism and Magnetic Materials*, **305**, 269 (2006).

[8]   C. Guillaud, "The properties of Mn-Zn ferrites and the physical processes governing them," *Proc. IEE*, **104B**, 165 (1957).

[9]   R. Valenzuela, *Magnetic Ceramics*, Cambridge University Press, Cambridge (1994).

[10]   F. Brailsford, *Physical Principles of Magnetism*, D. Van Nostrand Company Ltd., London (1966).

[11]   J. L. Snoek, "Dispersion and absorptions in magnetic ferrites at frequencies above Mc/s," *Physica*, **14**, 207 (1948).

[12]   M. A. Ahmed and M. A. El Hiti, "Electrical and Dielectric properties of $Zn_{0.8}Co_{0.2}Fe_2O_4$," *J. Phys.*, III France **5**, 775 (1995).

[13]   Y. Yafet and C. Kittel, "Antiferromagnetic arrangements in ferrites," *Physical Review*, **87**, 290 (1952).

[14]   P. B. Pandya, H. H. Joshi, R. G. Kulkarni, "Bulk magnetic properties of Co-Zn ferrites prepared by co-precipitation method," *Journal of material science*, **26**, 5509 (1991).

[15]   E. Cedillo, J. Ocampo, V. Rivera and R. Valenzuela, "An apparatus for the measurement of initial magnetic permeability as a function of temperature," *Journal of Physics E. Scientific Instrument*, **13**, 383 (1980).

[16]   R. Valenzuela, "A sensitive method for the determination of the Curie temperature in ferrimagnets," *Journal of Material Science*, **15**, 3137 (1980)

[17]   B. D Cullity, *Introduction to Magnetic Materials*, Addison-Wisley Publishing Company, Inc., California (1972).

[18]   S. Chikazumi, *Physics of Magnetism*, Jhon Wiley & Sons. Inc., New York (1966).

CHAPTER 6

CONCLUSIONS

6.1 Conclusions

The XRD pattern of $Co_{0.40}Zn_{0.60}Fe_2O_4$ and $Co_{0.20}Zn_{0.80}Fe_2O_4$ compositions clearly indicate single phase and formation of spinel structure. The lattice constant of $Co_{0.40}Zn_{0.60}Fe_2O_4$ is found to be 8.4528 Å while 8.4644 Å for $Co_{0.20}Zn_{0.80}Fe_2O_4$ samples. The increase in lattice parameter with increasing Zn content in these samples can be explained on the basis of the ionic radii. The radius of the Zn^{2+} (0.74 Å) is greater than that of the Co^{2+} (0.72 Å).

In this experiment we consider two series of compositions $Co_{0.40}Zn_{0.60}Fe_2O_4$ and $Co_{0.20}Zn_{0.80}Fe_2O_4$ respectively. In one series sintering time (5h) is constant and sintering temperature is variable and in other series sintering temperature ($1200^{\circ}C$) is constant and sintering time is variable. The density as a function of sintering temperature of the $Co_{0.40}Zn_{0.60}Fe_2O_4$ samples sintered for 5h increases as the sintering temperature increases from $1100^{\circ}C$ to $1250^{\circ}C$ and above $1250^{\circ}C$ the density decreases slightly. The $Co_{0.20}Zn_{0.80}Fe_2O_4$ samples sintered for 5h also show similar behaviour of changes to that of $Co_{0.40}Zn_{0.60}Fe_2O_4$ samples except that the density is found to be maximum at $1200^{\circ}C$. The density as a function of sintering time of the $Co_{0.40}Zn_{0.60}Fe_2O_4$ samples sintered at $1200^{\circ}C$ increases slowly as the sintering time increases from 0.2h to 1h and above 1h the density increases rapidly. On the other hand, the density as a function of sintering time of the $Co_{0.20}Zn_{0.80}Fe_2O_4$ samples increases rapidly as the sintering time increases from 0.2h to 1h and above 1h the density decreases slowly. The maximum density as a function of sintering time is obtained for the $Co_{0.40}Zn_{0.60}Fe_2O_4$ samples sintered for 15h while for $Co_{0.20}Zn_{0.80}Fe_2O_4$ samples it is obtained for 1h sintering time

During the sintering process, the thermal energy generates a force that drives the grain boundaries to grow over pores, thereby decreasing the pore volume and increasing the density of the materials. At higher sintering temperatures the density decreases, because the intragranular porosity increases as a result of discontinuous grain growth.

The discontinuous growth of grain rises with temperature, hindering the migration of the pore to the grain boundary and hence, contributing toward the reduction of the sintered density. There is an enlargement of grain size obtained for increasing Zn content. This is because of the fact that Zn promotes sintering, bringing about an increase in grain size.

The permeability value increases with increasing Co content in $Co_{1-x}Zn_xFe_2O_4$. With the increase of sintering temperature, T_s the real part of the initial permeability is found to increase at first and then decreases. In case of $Co_{0.40}Zn_{0.60}Fe_2O_4$ samples, μ_i' increases as the T_s increases up to $1250°C$ and above $1250°C$, μ_i' decreases. The $Co_{0.20}Zn_{0.80}Fe_2O_4$ samples show similar change of permeability to that of $Co_{0.40}Zn_{0.60}Fe_2O_4$ samples except that μ_i' is found to be maximum at $1200°C$. The initial permeability as a function of sintering time of the $Co_{0.40}Zn_{0.60}Fe_2O_4$ samples increases slowly as the sintering time increases from 0.2h to 1h and above 1h initial permeability increases rapidly. The maximum initial permeability is obtained for the sample sintered for 15h. On the other hand the initial permeability of the $Co_{0.20}Zn_{0.80}Fe_2O_4$ samples increases rapidly as the sintering time increases from 0.2h to 1h and above 1h initial permeability decreases slowly. The maximum initial permeability is obtained for the sample sintered for 1h.

we have observed that for both the compositions μ_i' is found to be maximum at optimum T_s (depending on sample composition). If the sintering temperature is higher than that of the optimum T_s, μ_i' decreases. It is possible that the samples sintered at higher sintering temperatures (> optimum T_s) may increase the number of pores within the grains which results in a decrease of permeability and also density. A sample with more uniform as well as highest density is obtained at $1200°C$ sintering temperature for $Co_{0.40}Zn_{0.60}Fe_2O_4$ composition sintered for 15h. The initial permeability is mainly affected by domain wall displacement or by wall bowing and changes with sintering density. Porosity and other defects do not affect the initial permeability if they are confined to the grain boundaries (intergranular defects) because thicker grain boundaries are preferred to increase the resistance and high resistance keep the eddy current losses minimum; otherwise, the initial permeability severely decreases since porosity within grains acts as pinning sites, reducing the volume swept by wall bowing or by wall

73

displacement. The initial permeability μ_i' is independent of frequency below the resonance frequency f_r, which is not observed in these samples within the measured frequency range (1KHz to 13MHz). Also the AC resistivity of these samples are very high compared with other ferrites which minimise the eddy current losses. For these reasons these types of ferrites are preferable for high frequency applications compared with other ferrites (i.e. $NiZnFe_2O_4$, $MnZnFe_2O_4$ etc.).

From the loss factor we have calculated the relative quality factor (or Q factor) for both compositions sintered at various temperatures and various dwell times. For inductors used in filter applications, the quality factor is often used as a measure of performance. It is observed that the sample sintered at $1300°C$ has highest Q value for $Co_{0.40}Zn_{0.60}Fe_2O_4$. The highest Q value for $Co_{0.40}Zn_{0.60}Fe_2O_4$ is found to be 2.25×10^3 at frequency 4MHz at $1300°C$ sintering temperature. The highest Q value for $Co_{0.20}Zn_{0.80}Fe_2O_4$ samples is not found between our frequency range (1KHz to 13MHz) because it exist above 13MHz frequency. So $Co_{0.20}Zn_{0.80}Fe_2O_4$ samples are suitable for very high frequency application.

The variation of magnetization as a function of temperature, $M(T)$ shows that the $Co_{0.20}Zn_{0.80}Fe_2O_4$ sample sintered at $1200°C$ for 5h undergo paramagnetic to ferrimagnetic transition at a temperature, T_c, 170K. From the $M-H$ curve, the magnetisation as a function of applied magnetic field, it is clear that at room temperature the sample $Co_{0.40}Zn_{0.60}Fe_2O_4$ is in ferrimagnetic state while the sample $Co_{0.20}Zn_{0.80}Fe_2O_4$ is in paramagnetic state. The values of T_c's are 330K. 351K, 374K and 397K for $Co_{0.40}Zn_{0.60}Fe_2O_4$ composition sintered at $1100°C$, $1200°C$, $1250°C$ and $1300°C$ for 5 hours respectively and 343K, 351K and 359K for the same composition sintered at $1200°C$ for 1h, 5h and 15 h, respectively.

It is noted that the samples of two compositions contain different Zn contents. It is observed that the T_c is lower when Zn content is higher. This is expected because of the inclusion of higher concentration of non-magnetic Zn in the materials. This is in harmony with the theoretical and experimental findings. It is also observed that the T_c is slightly increased with increasing sintering temperature.

The decrease of T_c with an increasing Zn content may be explained by a modification of the $A-B$ exchange interaction strength due to the change of the Fe^{3+} distribution between A and B sites. The decrease of the Curie temperature is due to the weakening of the $A-B$ interaction. This could be attributed to the increase in distance between the moments of A and B sites, which is confirmed by the increase in the lattice parameter with increasing Zn content. The larger distances between moments in samples $Co_{0.20}Zn_{0.80}Fe_2O_4$ leads to decrease the $A-B$ interaction relative to that of $Co_{0.40}Zn_{0.60}Fe_2O_4$ samples and consequently the T_c decreases. From this investigation, we may finally conclude that the highest permeability can be obtained by choosing the proper composition, sintering temperature (optimum T_s) and sintering time.